学位論文

Study on Structural Analysis in Layered
Superconductors using Synchrotron Radiation
X-ray Diffraction

（放射光 X 線回折を用いた構造解析による

層状超伝導体の研究）

2024 年 3 月

小林　天

# Abstract

This paper devotes two distinct yet interconnected areas of study in layered superconductors through the structural analysis with synchrotron X-ray diffraction. One is the relation between the superconducting properties and the crystal structure of $LaO_{0.5}F_{0.5}BiS_2$ substituted with Sn. Another is the relation between charge density wave and the surface and the bulk structure in $ZrTe_3$.

During the exploration of Sn-substituted $LaO_{0.5}F_{0.5}BiS_2$, a structural phase transition from the semiconducting $P4/nmm$ to the metallic $P2_1/m$ phase was discovered. This transition, induced by Sn substitution, is unprecedented in $BiS_2$ systems. This transition was accompanied by the bulk superconductivity with a transition temperature ($T_c$) of approximately 6 K. Furthermore, a filamentary superconducting phase with $T_c$ of approximately 8 K was observed, suggesting the potential for further enhancement of $T_c$ through elemental substitution. The improved transition temperature is related to the coexisting of $P2_1/m$ and $P4/nmm$ phases.

A comprehensive analysis of $ZrTe_3$ crystal structure revealed selective defects of approximately 5% at Te2 and Te3 sites. These findings provide insights into the charge density wave (CDW) and superconductivity in $ZrTe_3$. Real-space observations using STM/STS above the CDW transition temperature ($T_{CDW}$) revealed the existence of a faint modulation lacking phase coherence in either the CDW direction or its perpendicular counterpart. Notably, the Te defects on the sample surface exhibited a contrast-enhanced region of faint modulation, which is potentially linked to Friedel oscillations near $T_{CDW}$.

This research not only advances the understanding of Sn-substituted $LaO_{0.5}F_{0.5}BiS_2$ and $ZrTe_3$ but also sets the stage for future investigations into the intricacies of structural transitions and defects in superconducting materials.

# List of acronyms

STM: Scanning Tunneling Microscopy

STS: Scanning Tunneling Spectroscopy

CDW: Charge Density Wave

SC: Superconductivity

S-XRD: Synchrotron X-ray Diffraction

SEM: Scanning Electron Microscope

EPMA: Electron Probe Microanalyzer

EDX: Energy Dispersive X-ray spectrometer

WDS: Wavelength Dispersive X-ray Spectrometer

CP: Chemical Pressure

ARPES: Angle-Resolved Photoemission Spectroscopy

DOS: Density of State

LDOS: local DOS

# Contents

# Chapter 1

## 1 Introduction

In this thesis, I studied materials which show quantum-ordered phases, such as superconductivity and charge density wave(CDW). As an introduction, I describe superconductivity and CDW briefly in this chapter.

## 1.1 Superconductivity

Superconductivity is one of the macroscopic quantum mechanical phenomena. In addition to the well-known disappearance of electrical resistance below the superconducting transition temperature ($T_c$), it exhibits many unique properties. These properties have been utilized in many applications, and the material has been commercialized in wire, thin film, and bulk forms. Superconducting wires are used as magnets in linear motor cars and magnetic resonance imaging (MRI) measurements. Superconducting thin films are used in voltage standards and electromagnetic wave detectors. In bulk, they are used in quantum accelerators as cavity resonators. Thus, the phenomenon of superconductivity is widely used not only in research fields but also in industrial equipments and is indispensable for future society.

### 1.1.1 Zero electrical DC resistance

One of the most characteristic properties of superconductivity is the disappearance of electrical resistivity. Figure 1 (a) shows schematically the superconducting transition as the electrical resistivity changes with temperature. Although there are various definitions of $T_C$, in this paper, we define $T_c^{\text{onset}}$ and $T_c^{\text{zero}}$ as the temperature at which the electrical resistivity begins to decrease and the temperature at which the electrical resistivity becomes zero, respectively.
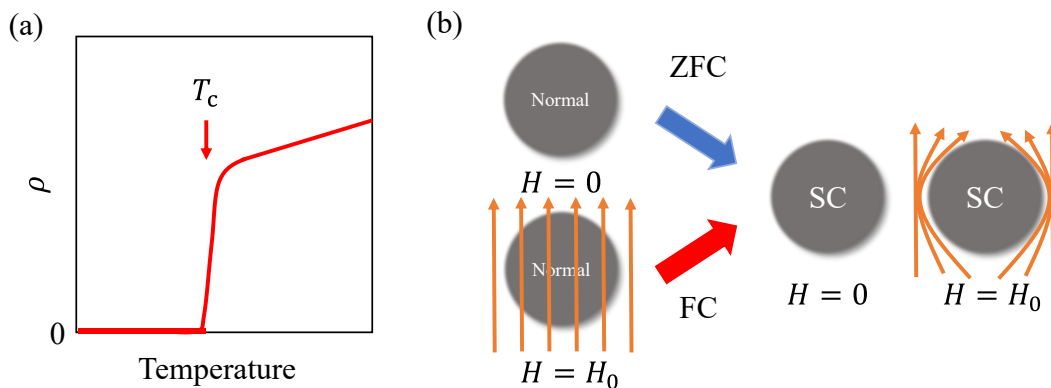


Fig. 1. (a) Schematic view of the behavior of electrical resistivity in a superconductor (b) Behavior of a superconductor under a magnetic field (ZFC: zero-field cool, FC: field cool)

## 1.1.2 Perfect diamagnetism

F. W. Meissner and R. Ochsenfeld precisely measured the magnetic flux distribution in superconductors in the superconducting state. They found that the superconductor never achieves a perfect electric conducting state and that the magnetic flux inside the superconductor is always zero. [1] This is one of the most characteristic properties of superconductors: perfect diamagnetism (Meissner effect). The Meissner effect is characterized by the magnetic flux inside the superconductor in the zero-field cool (ZFC) and field cool (FC) processes: The Meissner effect does not allow the magnetic flux to enter the superconductor in the ZFC process, but eliminate the magnetic flux in the FC process.
Figure 1 (b) shows schematically the flux change inside the superconductor in the ZFC and FC processes.

The zero electrical DC resistance and the Meissner effect are independent properties, and superconductivity is achieved by satisfying both. This indicates that the superconducting volume fraction is 100% in the magnetic susceptibility measurement, and this state is specifically called bulk superconductivity (SC).

In addition to bulk SC, there are other superconducting states that exhibit the zero electrical DC resistance and do not exhibit the perfect Meissner effect. In this case, the superconducting volume fraction is not 100%. Such superconductivity is called filamentary SC.

## 1.1.3 Theory of superconductivity

In this section, a theoretical interpretation of the superconductivity phenomenon is presented. First, I explain the phenomenological interpretation called London theory.

In 1935, F. W. London and H. London considered the phenomenon of superconductivity from an electromagnetic point of view.[2] They considered that the superconducting current in a superconductor was driven by a magnetic field rather than an electric field. They assumed that the Meissner effect is expressed in the following equation:

$$\nabla \times \boldsymbol{j} = -\frac{c}{4\pi}\frac{1}{\lambda_{\text{London}}^2}\boldsymbol{B}$$

$$\lambda_{\text{London}} = \sqrt{\frac{m^*c^2}{4\pi ne^{*2}}}$$

where $\boldsymbol{j}$ :superconducting current density, $c$ :light speed, $\boldsymbol{B}$ :magnetic flux density, $n$ :superconducting electron density, $e^*$ :superconducting electron charge, $m^*$:superconducting electron mass. $\lambda_{\text{London}}$ is the London's magnetic field penetration depth. Applying Ampere's law, the following equation was obtained:

$$\nabla^2 \boldsymbol{B} = \frac{\boldsymbol{B}}{\lambda_{\text{London}}^2}$$

The solution of this equation is derived as follows:

$$\boldsymbol{B}(r) = \boldsymbol{B}(0) \exp\left(-\frac{r}{\lambda_{\text{London}}}\right)$$

The position at $r = 0$ is defined as the surface of the superconductor, and a positive increase in r indicates the penetration into the superconductor. It is also assumed that a magnetic field is applied parallel to the surface. According to this relationship, the magnetic field decays exponentially inside the superconductor.

There are two types of breakdown of superconductivity with respect to magnetic fields. The first is a type-I superconductor, in which the superconducting state is completely destroyed when the magnetic field is over $H_c$. The second is a type-II superconductor, in which the superconductivity is gradually destroyed when the magnetic field is increased over a certain field ($H_{c1}$): the magnetic flux begins to penetrate into the superconductor and the normal and superconducting states are mixed. The magnetic field at which the superconducting state is completely destroyed by further increase in the magnetic field is called $H_{c2}$.

Another phenomenological theory of the superconductivity phenomenon from a different perspective was proposed in 1950, V. L. Ginzburg and L. D. Landau explained the superconductivity phenomenon from a thermodynamic point of view (GL theory).[3] It is known that superconductivity is thermodynamically a single phase and the transition to the superconducting state corresponds to a second-order phase transition. Therefore, the V. L. Ginzburg and L. D. Landau explained the superconducting transition in the framework of a general second order phase transition.

In second order phase transition, the order parameter $\Psi$ is defined as the degree of ordering, which is $\Psi = 0$ above the transition temperature and $\Psi \neq 0$ below the transition temperature. The GL theory defines the order parameter as a macroscopic wave function as follows:

$$\Psi(\boldsymbol{r}) = f(\boldsymbol{r}) \exp(i\theta(\boldsymbol{r}))$$

$|\Psi|^2$ gives the number of superconducting electron densities. Using this order parameter $\Psi$ and considering the Helmholtz free energy, we can obtain the following equation:

$$F_{\text{S}} = F_{\text{N}} + \alpha|\Psi|^2 + \frac{\beta}{2}|\Psi|^4$$

where $F_{\text{S}}$: free energy in the superconducting state, $F_{\text{N}}$: free energy in the normal conducting state, $\alpha, \beta$: constants. When an external magnetic field $H_0 < H_c$ exists, the term $|\nabla\Psi|^2$ is added to the above equation. In addition, the effect of eliminating the magnetic flux is also added, resulting in the following equation:

$$F_{\mathrm{S}} = F_{\mathrm{N}} + \alpha|\Psi|^2 + \frac{\beta}{2}|\Psi|^4 + \frac{1}{2m^*}\left|\left(-i\hbar\nabla - \frac{e^*}{c}\boldsymbol{A}\right)\Psi\right|^2 + \frac{H_0^2}{8\pi}$$

The ordered phase can be determined by minimizing $F_{\mathrm{S}}$. Then, the following equation is obtained by applying variational method regarding the order parameter and magnetic field.

$$\nabla \times \nabla \times \boldsymbol{A} = \frac{4\pi}{c}\boldsymbol{J}_{\mathrm{S}}$$

$$\left[\frac{1}{2m^*}\left(-i\hbar\nabla - \frac{e^*}{c}\boldsymbol{A}\right)^2 + \alpha + \beta|\Psi|^2\right]\Psi = 0$$

$$\left(\boldsymbol{J}_{\mathrm{S}} = \frac{ie^*\hbar}{2m^*}\left[\Psi^*(\nabla\Psi) + (\nabla\Psi^*)\Psi - \frac{e^{*2}}{mc}|\Psi|^2\boldsymbol{A}\right]\right)$$

These equations are called the GL equations.

When there is no external magnetic field ($\boldsymbol{A} = 0$), the following equation is obtained from the GL equation:

$$\alpha\Psi_0 + \beta\Psi_0^3 = 0$$

$$\Psi_0^2 = 0, -\frac{\alpha}{\beta}$$

Returning to the definition of the order parameter, it is necessary to satisfy $\Psi = 0$ above the transition temperature and $\Psi \neq 0$ below the transition temperature. Thus, $\alpha$ and $\beta$ are assumed as:

$$\alpha(T) \sim \alpha_0\left(\frac{T - T_{\mathrm{c}}}{T_{\mathrm{c}}}\right), \alpha_0 \equiv \alpha'(T_{\mathrm{c}})T_{\mathrm{c}}$$

$$\beta(T) \sim \beta > 0$$

The order parameter $\Psi_0$ is as follows:

$$\Psi_0 = 0 \ (T > T_{\mathrm{c}}), -\frac{a_0}{\beta}\left(\frac{T - T_{\mathrm{c}}}{T_{\mathrm{c}}}\right)(T < T_{\mathrm{c}})$$

By writing $\Psi$ as $\Psi_0 f$, we obtain the following equation:

$$(-\xi^2(T)\nabla^2 f + f - f^3)\Psi_0 = 0$$

$$\xi^2(T) \equiv \frac{\hbar^2}{2m^*\alpha_0}\left(\frac{T_{\mathrm{c}}}{T_{\mathrm{c}} - T}\right)$$

In this equation, $\xi$ has a length dimension, indicating that spatial change of $\Psi_0$. This $\xi$ is called the coherence length at $T \ll T_{\mathrm{c}}$.

When the change in the order parameter is sufficiently small and $\nabla\Psi = \nabla\Psi^* = 0$, the current density in the GL equation becomes the following equation:

9

$$J_S = -\frac{e^{*2}n_S}{m^*c}A = -\frac{c}{4\pi}\frac{1}{\lambda_{London}^2(T)}A$$

Taking a rotation in this equation gives the London equation. $\lambda_{London}$ is called the London penetration depth, and its temperature dependence is the following equation:

$$\lambda_{London}^2(T) = \frac{m^*c^2\beta}{4\pi e^{*2}\alpha_0}\left(\frac{T_c}{T_c - T}\right)$$

Both the London penetration depth and coherence length have characteristic lengths. Both lengths increase when the temperature $T$ approaches $T_c$ from lower temperatures and diverge at $T=T_c$. Let $\kappa$ be the ratio of these two lengths:

$$\kappa = \frac{\lambda(T)}{\xi(T)} = \frac{m^*c}{e^*\hbar}\sqrt{\frac{\beta}{2\pi}}$$

This quantity is a temperature-independent value called the GL parameter, which is substance-specific.

Now, let's move to the microscopic theory: BCS theory by J. Barden, L. Cooper, and R. Schrieffer.[4] Prior to BCS theory, studies of isotope effects suggested that lattice vibrations are closely related to superconductivity phenomena. An intuitive understanding of the electron-lattice interaction is that electrons distort the periodic arrangement of the surrounding metal ions. In other words, the electron-lattice interaction can be understood as the emission and absorption of phonons by electrons.

For example, consider a process in which two electrons A and B exist at $E_F$, and the phonon emitted by electron A is absorbed by electron B. In this process, if the energy between electrons A and B is sufficiently small compared to the energy of the phonon, there is an attractive force between electrons A and B. This pair is called the Cooper pair. When an electron exists as a Cooper pair, it loses its Fermi particle nature and becomes a Bose particle: Thus, many Cooper pairs condense into a single quantum state.

In the superconducting state where Cooper pairs are formed, a gap is opened above and below $E_F$ with $\Delta(T)$. This energy gap is called the superconducting gap, which decreases with increasing temperature and disappears at $T = T_c$, indicating that more than $2\Delta$ of energy is required to break the Cooper pairs. This theory successfully explained electromagnetic and thermal properties of superconductors.

The BCS theory, which uses electron-phonon interaction as origin of the electron pairing, predicted that the upper limit of $T_c$ is approximately 40 K. However, $T_c$ higher than 40 K has been observed in copper oxide-based and iron-based superconductors. [5,6] This indicates the possible existence of other pairing mechanisms than electron-phonon interaction, for example fluctuation of spins or orbits. Thus, for understanding and enhancement of $T$c of superconductors, it is necessary to investigate various superconductors from different viewpoints.

## 1.2 Charge density wave

In this section, I explain the charge density wave (CDW), which is often discussed in relation to superconductivity. CDW is one of the quantum-ordered phases responsible for the electron-phonon coupling. A metal-insulator transition occurs at the phase transition to CDW state occurs.

### 1.2.1 Theory of charge density wave

In 1940, R. Peierls described the mechanism for the appearance of the CDW, known as the Peierls instability.[7] He first predicted the appearance of the CDW state owing to the instability in one-dimensional electronic systems.

The charge density $\rho(q)$ is proportional to the periodic potential $V_q$ of the crystal lattice as follows:

$$\rho(q) = -V_q \chi(q)$$

where the proportionality coefficient $\chi(q)$ is the charge susceptibility. $\chi(q)$ is a function of the wave vector and is expressed as the following formula using the Fermi distribution functions $f_k$ and $f_{k+q}$ and energies $E_k$ and $E_{k+q}$ in the wave vector $k$ and $k + q$.

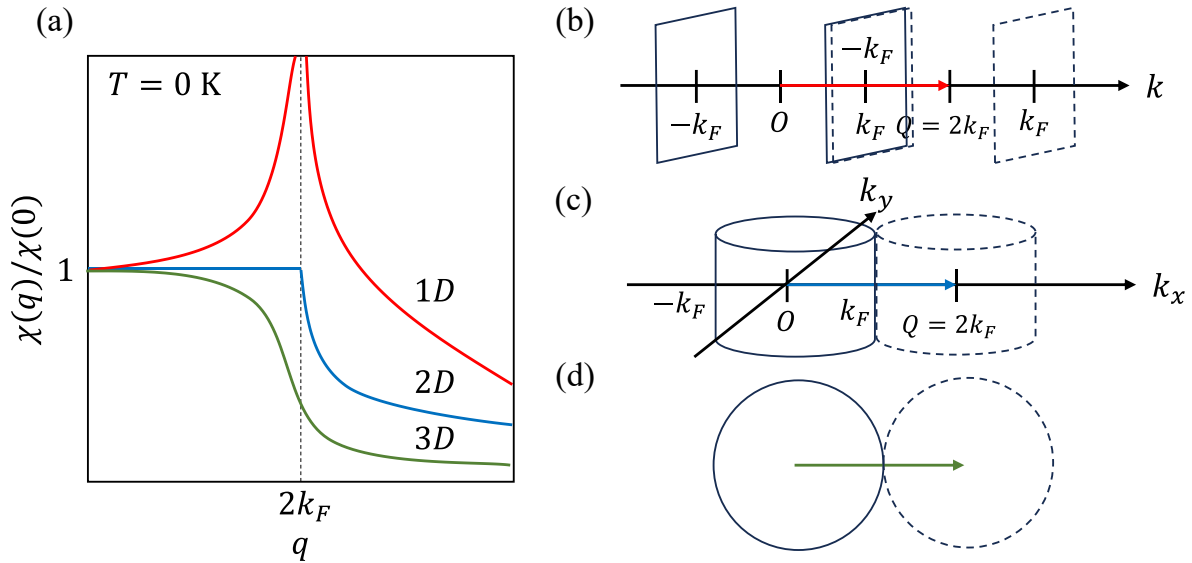$$\chi(q) = \frac{1}{V_q} \Sigma_k \frac{f_{k+q} - f_k}{E_k - E_{k+q}}$$



Fig. 2. Dependence of the charge susceptibility and Fermi surface on dimensionality. (a) Charge susceptibility depending on wave vector and the dimensionality shown by red, blue, and green curves for one-, two-, and three-dimensional materials, respectively. (b)-(d) Schematic illustration of the 1D, 2D, and 3D Fermi-surfaces.

Figure 2 (a) shows the wave vector dependence of charge susceptibility as red, blue, and green curves for 1D, 2D, and 3D cases, respectively. As the dimension of the electron system decreases, the divergence of the charge susceptibility at $k = 2k_F$ appears, indicating that the electron system becomes unstable. Furthermore, the modulation of the charge density becomes more significant. This is explained by the nesting of the Fermi surfaces: as shown in Fig. 2 (b). Because the overlap of the Fermi surfaces at $k = 2k_F$ is large, the nesting is good for one-dimensional electron systems. In contrast, for the 2D and 3D Fermi surfaces shown in Fig. 2 (c) and (d), respectively, the overlap of the Fermi surfaces is worse than that for the 1D case. Even in the case of the same dimension, when the nesting of the Fermi surfaces is poor, the modulation of charge density is small, and the formation of the CDW is not expected. Thus, the CDW is strongly dependent on the shape of the Fermi surface.

Figure 3 shows a schematic of the Peierls transition in 1D material.[8] In the free-electron model, as shown in Fig. 3 (a), there is no energy gap in the band dispersion, and the charge density is uniform. The introduction of a periodic potential owing to the atomic lattice creates an energy gap at the zone boundary, as shown in Fig. 3 (b). Furthermore, by taking into consideration the electron-phonon coupling and assuming good nesting of the Fermi surfaces, the modulation of the charge density corresponding to the wave vector $2k_F$ occurs. The atomic lattice was also distorted by the same wave vector. As shown in Fig. 3 (c), an energy gap is formed near to $E_F$, and the energy of the electron system decreases. In the Peierls mechanism, the CDW state appears when the decrease in electron energy is balanced by an increase in the lattice energy. Corresponding to the atomic lattice distortion, as shown in Fig. 3 (d), phonon
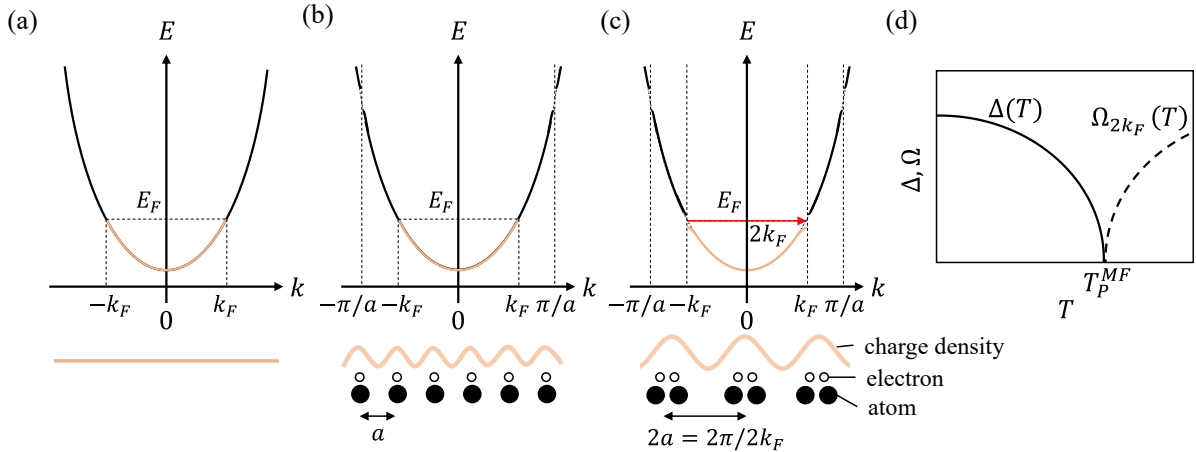


Fig. 3. Schematic diagram of the Peierls transition. [7] (a)-(c) Band structure, charge density, and atomic lattice are shown. (a) Diagram of the band structure in the case of a 1D free-electron gas. (b) Diagram of the band structure in the case of a 1D atomic chain. The energy gap emerges at $k = \pm\pi/a$ owing to the 1D atomic chain. (c) Diagram of the band structure in the case of 1D material with CDW state. The charge density is modulated by the periodicity corresponding to the Fermi wave vector. The energy gap emerges because of the CDW transition in addition to the 1D atomic chain. (d) Temperature dependence of the order parameter $\Delta$ and the soft phonon frequency $\Omega_{2k_F}$ on the Peierls transition.

frequency $\Omega_{2k_F}$ softening, called Kohn anomaly, occurs. Phonon softening occurs from temperatures higher than the Peierls transition temperature ($T_P^{MF}$).

The Peierls transition is a second-order phase transition with the energy gap $\Delta$ as the order parameter, similar to superconductivity, and $\Delta$ develops below $T \sim T_P^{MF}$ as shown in Fig. 3 (d).

Both CDW and superconductivity are the phenomena involving electrons at the Fermi energy. Therefore, there is competition between the CDW and superconductivity. Such a competition has been suggested in $ZrTe_3$, which is the subject of this paper.


## 1.3 Organization of this thesis

Crystal structure is the most basic and important factor in the recognition of physical properties. When the crystal structure is low-dimensional, such as a layered structure, electronic states become low-dimensional. In low-dimensional materials, quantum phases such as exotic superconductivity and charge density wave, and strongly correlated states emerge. The physical properties of these quantum phases are also greatly affected by imperfections such as local crystal structures, atomic substitution, and/or defects. Therefore, in addition to measurements of transport phenomena, structural analysis by diffraction experiments in reciprocal space and complementary structural observations in real space are required to elucidate the physical properties of these quantum phases. In particular, synchrotron X-ray diffraction measurements allow us to investigate the amount and site dependence of atomic substitutions and defects with higher precision and resolution than laboratory X-ray.

In this paper, we investigate the crucial relationship between crystal structure and ordered state in two layered superconductors, $LaO_{0.5}F_{0.5}BiS_2$ and $ZrTe_3$ by detailed structural analysis using synchrotron radiation X-ray and scanning tunneling microscopy and spectroscopy (STM/STS).

In $LaO_{0.5}F_{0.5}BiS_2$, transport phenomena measurements and crystal structure analysis were performed to investigate the improvement of superconducting properties in $LaO_{0.5}F_{0.5}BiS_2$ by substituting Bi sites with Sn. We found partial substitution for a few percents Sn induced the structural transition and realized the large enhancement of $T$c for the first time.

In $ZrTe_3$, charge density wave (CDW) exists. We observed CDW above CDW transition temperature by STM. The observed modulation was strongly affected by the surface defects. To elucidate the observed phenomena on the surface was valid in the bulk, the defect in the bulk was examined by synchrotron X-ray diffraction measurements. We found site selective defects of the constituent atoms and large atomic displacement parameters for the first time.

Chapter 2 describes the basic principles of synchrotron X-ray diffraction and STM/STS measurements, which are the experimental techniques used in this study. An

overview of the experimental techniques, including the actual apparatus used, and methods for analyzing the measurement data will be described.

In Chapter 3, we will describe the study on $LaO_{0.5}F_{0.5}BiS_2$, focusing on the improvement of superconducting properties and changes in the crystal structure observed by Sn substitution.

In Chapter 4, we will describe the study on $ZrTe_3$, focusing on the effects of defects on the CDW.

In Chapter 5, we summarize these two studies and present future prospects.

# Chapter 2

## 2 Measurement methods

This chapter describes the experimental techniques and equipment used in this study.

## 2.1 Synchrotron X-ray diffraction

X-ray diffraction experiment is a powerful technique for studying crystal structures. X-ray is a type of electromagnetic wave that interact with electrons around atoms. When X-ray penetrates into a material, the interaction between the X-ray and the electrons causes the electron oscillation, which in turn causes the surrounding electric field created by the electron oscillation. The interference of these oscillating electric fields produces scattered X-ray radiation. In diffraction experiments, the position and intensity of the scattered X-ray can be used to decide the crystal structure. From the positional information of the scattered X-ray, the crystal system and the lattice constant can be determined. On the other hand, the atomic spices and coordinates of the constituent atoms can be determined from the intensity of the scattered X-ray.

## 2.1.1 Synchrotron X-ray

Characteristic X-ray of Cu and Mo are commonly used in a laboratory as a source of X-ray. Characteristic X-ray is emitted when a metal is subjected to high energy, the electrons of the constituent elements are ejected, and the outer shell electrons fall into the vacancies that are created at that time. In addition, there is not only one type of characteristic X-ray, but also includes secondary characteristic X-ray such as $K_\beta$ in addition to the dominant $K_\alpha$.

Figure 4 shows a schematic illustration of the generation principle of synchrotron radiation X-ray. Synchrotron radiation X-ray has the following five main features.

1) $10^8 \sim 10^{11}$ times brighter than a laboratory X-ray system.

2) Single-wavelength X-ray is extracted.

3) Selectable wavelength of X-rays.

4) High spatial coherence

5) X-ray beam is polarized.

Because of these characteristics, it is possible to perform a wide variety of experiments with precision. To generate synchrotron X-ray, it requires many facilities, including an accelerator that accelerates electrons to nearly the speed of light, powerful electromagnets for bending electrons, and radiation protection equipment. Thus, for synchrotron X-ray experiments, large synchrotron radiation facilities such as
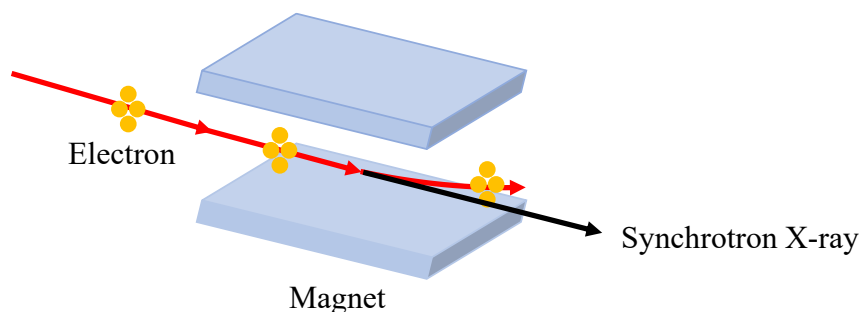
Fig. 4. Schematic illustration of synchrotron radiation X-ray generation mechanism

SPring-8, Photon Factory, and NanoTerasu are used. The experiments in this paper were conducted at SPring-8 beamline BL02B1 and BL02B2.

## 2.1.2 Experimental apparatus

This section describes the actual experimental apparatus used.

## 2.1.2.1 Detector

Diffraction experiments were performed at SPring-8 beamline BL02B1 and BL02B2 for single-crystal and polycrystal measurements, respectively.

In BL02B1 for single crystal measurements, a photon-counting detector PILATUS was used. In this device, X-ray detector elements ($0.172mm \times 0.172mm$) made of CdTe semiconductors are laid out in an array. The number of photons is counted by reading the current generated when an X-ray photon strikes the semiconductor eleme nt. Since a current readout circuit is installed in each element, high-speed readout is possible. The system is also free from dark current and readout noise. The dynamic range is $10^6$, the pixel size is $0.1mm \times 0.1mm$, and the detection area is $169mm \times 180mm$, respectively.

In BL02B2 for polycrystal measurements, a photon coefficient type detector MYTHEN was used. This detector uses the same mechanism as PILATUS. On the other hand, the detector is a one-dimensional detector because the $\theta - 2\theta$ method is used in the polycrystalline experiments. $2\theta$ range is 1~75° with a resolution of 0.006°.

Both detectors are much more powerful than those used in a laboratory to take advantage of the characteristics of synchrotron radiation X-ray and can give very precise data that cannot be obtained in a laboratory.

## 2.1.2.2 Monochromator

A monochromator is an indispensable optical device for beam lines. The principle of spectroscopy is quite simple: Bragg reflection in a perfect single crystal. The monochromator can control X-ray with a specified energy (wavelength) and energy width. Two monochromators (double-crystals monochromator) are also responsible for controlling the optical axis of the X-rays incident on the sample and for focusing the beam.

16

In BL02B1 and BL02B2, Si single-crystal is used as monochromator. In this case, the Bragg angle can be selected in the range of 3~27°. Therefore, considering Bragg's law, selecting the Bragg angle means selecting the wavelength.

## 2.2 Scanning tunneling microscopy

Scanning Tunneling Microscopy and Spectroscopy (STM/STS) is an instrument for characterizing the surface morphology and electronic state with the atomic resolution. By applying a voltage between the sample and the sharply pointed probe (Tip), which is brought close to the sample at a few Å to a few nm, tunneling current flows. By observing the change of the tunneling current when the tip is scanned on the sample surface, one can obtain the surface morphology. Since its invention by G. Binning and H. Rohrer, it has been used in various fields.[9] In particular, STM has contributed to the elucidation of quantum phenomena because of its ability to obtain electronic states of surfaces with atomic resolution. In this section, we explain tunneling currents, the actual experimental setup used, and the acquisition methods of topographic imaging and tunneling spectroscopy.

## 2.2.1 Tunneling Current

Optical microscopes, which are commonly used, obtain a magnified image of an object by focusing light through the lens. In contrast, STM observes an object by measuring the tunneling current between a metal probe and the object. In principle, STM uses tunneling current to obtain an atomic-scale image with higher resolution than optical microscopes, which are limited by the diffraction limit.

Tunneling current is a current that flows owing to the tunneling effect. The tunneling effect is a phenomenon that a particle passes through a potential barrier between two states. In the case of tunneling current, this particle is an electron. In a normal STM measurement, this potential barrier corresponds to a vacuum barrier. When the distance between the sample and the probe is brought to a few Å, the probability of electrons tunneling through the potential barrier increases and ~~a~~ the tunneling current flows between the tip and the sample. A schematic illustration is shown in Fig. 5 (a). In the following, we consider the case where the positive bias voltage is applied to the
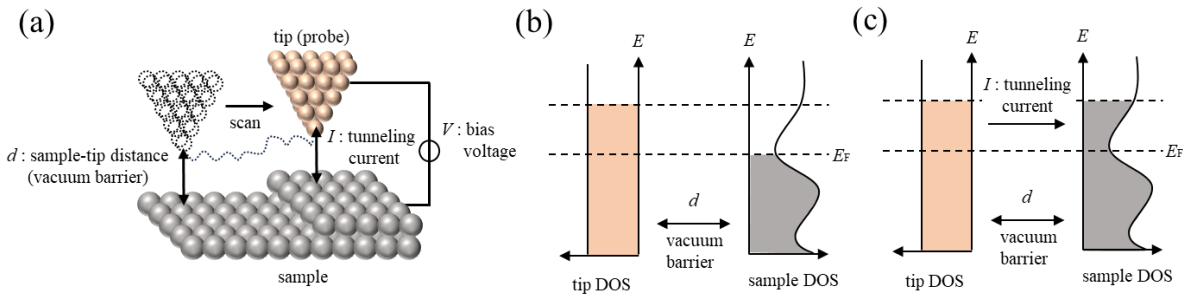


Fig. 5. (a) Schematic illustration of the tunneling current between the tip and a sample. (b),(c) DOS of the tip and the sample before and after tunneling current flows, respectively.

sample. In this case, $E_F$ of the sample is lower than that of the tip as shown in Fig. 5 (b). Therefore, electrons flow from the tip to the sample as shown in Fig. 5 (c).

The tunneling current from the Tip to the sample is described as follows.

$$I_{t \to s} = -\frac{4\pi e}{\hbar} \int_{-\infty}^{\infty} |M|^2 \left[N_t(E - eV)f(E - eV)\right] \left[N_s(E)\big(1 - f(E)\big)\right] dE$$

where $e$: elementary charge, $N_t$: DOS of the tip, $N_s$: DOS of the sample, $f$: Fermi distribution function, $M$: tunnel matrix element. $|M|^2$ is the tunneling probability. The tunneling current $I_{s \to t}$ from the sample to tip can be obtained by replacing the terms in the Fermi distribution function in the above equation.

Because the measured tunnel current is the sum of $I_{s \to t}$ and $I_{t \to s}$, the following equation is obtained.

$$I_{mes} = I_{s \to t} + I_{t \to s} = -\frac{4\pi e}{\hbar} \int_{-\infty}^{\infty} |M|^2 \left[N_t(E - eV) N_s(E)\right] \left[f(E - eV) - f(E)\right] dE$$

If the bias voltage is smaller than the work function, the tunneling probability can be assumed to be energy independent. If the DOS of the tip is energy-independent and constant, the tunneling current can be described as follows.

$$I_{mes} = -\frac{4\pi e}{\hbar} |M|^2 N_t \int_{-\infty}^{\infty} N_s(E) \left[f(E - eV) - f(E)\right] dE$$

The tunneling probability can be written as follows if the wave function of the tip-tip atom is isotropic.

$$|M|^2 \propto \exp\left(-\frac{\sqrt{8m\phi}}{\hbar} d\right)$$

where $m$: mass of electrons, $\phi$: average work function, $d$: distance between the tip and the sample.

At extremely low temperatures, the Fermi distribution function can be approximated by a step function because the thermal excitation of electrons is small. Therefore, at extremely low temperatures, the tunneling current can be approximated as follows.

$$I_{mes} \propto \exp\left(-\frac{\sqrt{8m\phi}}{\hbar} d\right) \int_0^{eV} N_s(E) dE$$

Thus, the magnitude of the tunneling current varies exponentially with the distance between the tip and the sample. The ability of STM to obtain atomic-level surface structure and electronic states is realized by this sensitivity of the tunneling current.

## 2.2.2 Experimental setup

This section describes the equipment actually used in the experiments.

STM/STS measurements were performed at 4.2 and 80 K. To cool the STM, a vacuum tube with an STM head attached was used at an internal pressure of

approximately $1 \times 10^{-7}$ Torr. This was inserted into a dewar vessel. Pure helium gas of several torr is then introduced into the vacuum tube as the exchange gas. The dewar was placed on an anti-vibration stage to avoid vibration noise.

Liquid helium was used for cooling the sample down to 4.2 K, and liquid nitrogen was used for cooling the sample down to 80 K. The specimens were placed in the vacuum tube. The clean surface of the sample was obtained by cleavage in a vacuum tube at the temperature of the measurement.

## 2.2.2.1 Preparation of tip

Among several types of tips, Au tips were used in this study. Fig. 6 (a) and (b) show the circuit diagram for making the Au tip and the actual process of making the Au tip, respectively. The circuit was composed of the Au wire as the anode and the Pt ring as the cathode at 4V, 0.05A. Mixture of $HCl:C_2H_5OH=1:1$ was used as the solution for electropolishing. Au wire and Pt ring are submerged in the mixture in a petri-dish. After that, the lower part of the Au wire dropped off from the surface of the solution to obtain a sharp Au tip.

The prepared Au tips were then rinsed with ion-exchanged water at 100°C and washed with acetone before use.
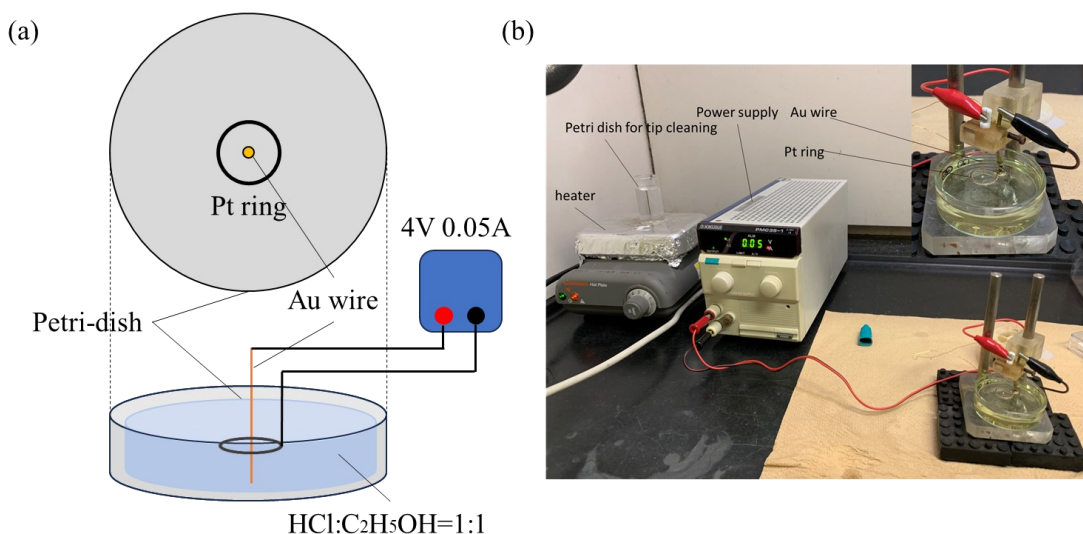


Fig. 6. (a) Circuit diagram for creating an Au tip, (b) Actual Au tip preparation

## 2.2.2.2 Driving and measuring systems

Piezoelectric elements were used to bring the tip closer to the sample. Figure 7 (a) shows a schematic of the STM head. The coarse movement mechanism is shown in Fig. 7 (b): the triangular prism on which the tip is mounted is sandwiched between six
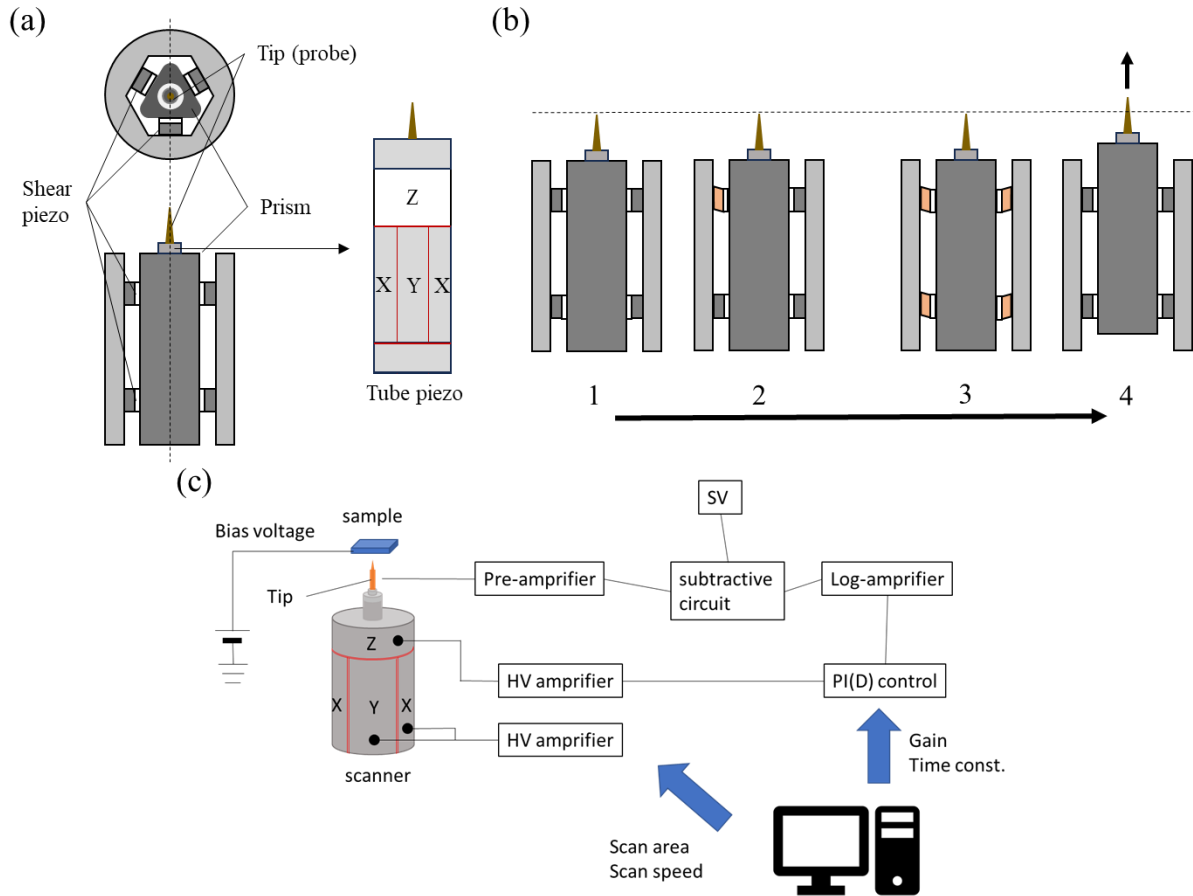
Fig. 7. Schematic illustrations of STM. (a) STM head (b) the course motion of the STM tip. (c) STM/STS measuring circuit.

shear piezos. Two piezos are placed on each of the three faces of the triangular prism. In the first stage 1, all shear piezos are discharged. In stage 2, each shear piezo is charged and slip one by one along the triangular prism. In stage 3, all shear piezos have slipped. In the fourth stage, all the piezo are discharged, and the prism moves up. This sequence of events is repeated until the tunneling current flows.

Next, I explain the fine movement drive that scans the sample surface at the atomic level. In the fine movement drive, a tube piezo placed inside a triangular prism is used. By applying voltage to the tube piezo from each direction, the tube prism is bent, which enables the fine movement of the tip.

The circuit for STM measurements and a schematic diagram of the STM/STS measurement system is shown in Fig. 7 (c). Because the magnitude of the tunnel current is several pA to several nA, a preamplifier is used to amplify the current value. When the tunnel current reaches a predetermined value (setpoint), the coarse approach motion by the pan-type drive system stops.[10] All STM measurements in this paper are performed in constant current mode, with a closed feedback loop to keep the tunnel current constant. The sample surface was scanned using a tube piezo-based fine motion system as described in above section. By applying a high voltage to the tube

piezo, the tip could be moved over a range of several hundred nm. The value of the voltage applied in each direction was controlled by a computer.

## 2.2.3 Measuring method

In this section, topographic imaging and spectroscopy in STM/STS measurements are described.

## 2.2.3.1 Topographic imaging

To give the real-space structure of a sample surface in STM measurements, there are two ways to scan the sample surface. One is called constant current mode, in which the probe is scanned while feedback is applied, keeping the tunneling current between the probe and the sample constant and varying in height. In this measurement method, the voltage applied to the piezo in the Z direction is recorded as a function of $(x, y)$. The other method is called constant height mode, in which the tip height is kept constant while scanning. In this measurement method, the value of the tunnel current is recorded as a function of $(x, y)$. In this paper, the former constant-current mode was used to image the sample surface structure.

## 2.2.3.2 Spectroscopy

The local DOS for each position on the sample surface is a function of position $(x, y)$ and energy. By fixing the tip position at a certain position and sweeping the bias voltage, the value of the tunnel current changes according to the value of DOS. In this case, the distance between tip and sample is initially set to the height at which the tunnel current flows at a set value.

Differentiating the *I-V* curve with the bias voltage gives the following equation.

$$\frac{dI_{mes}(x, y, z, V)}{dV} = f(z)N(x, y, z, eV)$$

where $f(z)$ is a function of the distance z between tip and sample. As can be seen from this equation, *dI/dV* gives a value proportional to the local DOS. The *dI/dV* map reflects the spatial dependence of the DOS and is a method to know the spatial variation of the electronic state.

# Chapter 3

## 3 Enhancement of superconductivity and structural instability by Sn substitution in LaO$_{0.5}$F$_{0.5}$BiS$_2$

In this chapter, I will discuss enhancement of superconductivity and structural instability in Sn substituted LaO$_{0.5}$F$_{0.5}$BiS$_2$.

## 3.1 Introduction

BiS$_2$-based superconductors discovered by Mizuguchi *et al.* have a layered structure consisted of an insulating blocking layer and a conducting layer composed of BiS$_2$.[11] Various combinations of blocking and conducting layers can be possible, resulting in a diverse family of superconductors.[12,13] The crystal structure is similar to that of cuprate high-$T_c$ superconductors or iron-based superconductors, and the mechanism of superconductivity in BiS$_2$-based superconductors has been the subject of much interest and research.

Among BiS$_2$-based superconductors, $R$OBiS$_2$ ($R$: rare-earth element) is the most studied one. It belongs to the tetragonal crystal system and has a structure consisting of the BiS$_2$ conducting layer and the $R$O blocking layer, with various rare-earth elements in the $R$ site (Fig. 8).

Superconductivity is realized by carrier doping and the superconducting transition temperature varies depending on the amount of the carriers.[11,14–19] Maximum $T_c \sim$ 2.5 K is achieved at about 50% substitution of O by F in LaOBiS$_2$.[14] The results of the band calculations of LaOBiS$_2$ and LaO$_{0.5}$F$_{0.5}$BiS$_2$ were performed by B. Li *et al.*[20] Figures 9 (a) and (b) show the results of the band calculations for LaOBiS$_2$
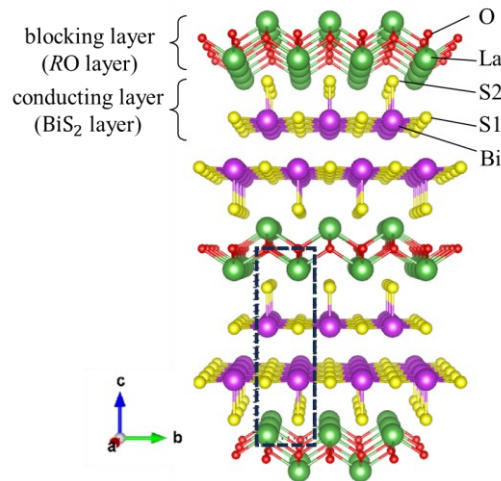


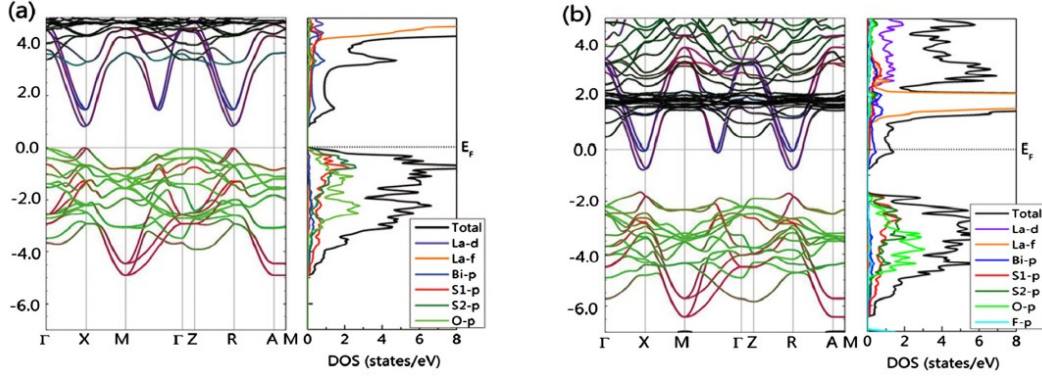Fig. 8. Crystal structure of $R$OBiS$_2$

Fig. 9. ©2013 The Europhysics Letters (EPL101,47002). Calculated band structure and density of states of $LaO_{1-x}F_xBiS_2$ for $x = 0$ (a), 0.5 (b), and 1 (c), with the orbital character indicated by different colors: Bi-$p$ (blue), S1-$p$ (red), and O-$p$ and S2-$p$ (green).

and $LaO_{0.5}F_{0.5}BiS_2$, respectively. They show that $LaOBiS_2$ has an insulating-like band structure, $LaO_{0.5}F_{0.5}BiS_2$ has states at the $E_F$ and becomes metallic. At the $E_F$, the conduction bands due to the Bi-$p$ and S1-$p$ states dominate.

It has been reported that the superconducting properties change significantly under hydrostatic pressure. Polycrystalline $LaO_{0.5}F_{0.5}BiS_2$ shows a semiconducting temperature dependence of the electrical resistance, and filamentary superconductivity at around 2.5 K under ambient pressure. With application of hydrostatic pressure, the crystal structure changes from tetragonal to monoclinic as shown in Fig. 10. The temperature dependence of the electrical resistivity becomes less semiconducting under hydrostatic pressure, and $T_c$ increases discontinuously to about 10.7 K around 0.7 GPa.[21] This $T_c$ is the highest value among $BiS_2$-based superconductors. In addition, samples annealed under high pressure show $T_c$ as high as that under pressure even under ambient pressure.[16,17] This is believed to be due to the fact that the crystal structure under high pressure is retained even under ambient pressure. Thus,
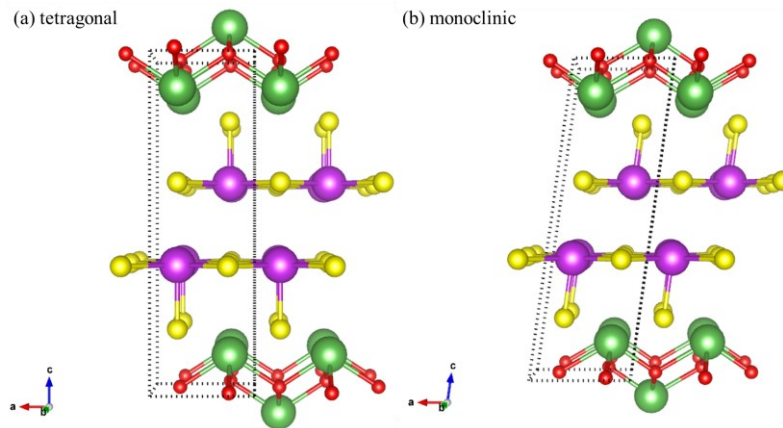


Fig. 10. $2 \times 2 \times 1$ unit cells for the (a) tetragonal $P4/nmm$ model at 0.4 GPa and (b) monoclinic $P2_1/m$ model at 3.8 GPa, viewed from the ac-planes. The Bi–Bi distance at the center of the cell was 3.70 Å. [21]

23

the change in the crystal structure is thought to play a significant role in the superconducting properties.

Changing the rare-earth element at $R$ site also affects the superconducting transition temperature. For example, in $LaO_{0.5}F_{0.5}BiS_2$, the superconductivity is filamentary and the $T_c$ is rather low, whereas in $NdO_{0.7}F_{0.3}BiS_2$, bulk superconductivity and rather high $T_c$ appears.[22] This has been explained by the fact that the difference in ionic radii of rare-earth ion causes the chemical pressure (CP) to the conducting layer.[17]

Figure 11 shows an example of the chemical pressure resulting from elemental substitutions. When Ce (ionic radius: 114 pm) is substituted by Nd (ionic radius: 112 pm), the substitution of the element with the smaller ionic radius decreases the volume of the blocking layer, resulting the shrink of the conducting layer. Therefore, CP is generated in the direction indicated by the red arrow in the figure.

This effect has also been confirmed by the substitution of chalcogen elements in the conducting layer. [21,24] When Ch site is replaced with Se (ionic radius: 198 pm) from S (ionic radius: 184 pm), the in-plane lattice constant increases. However, because the composition of the blocking layer is unchanged, the lattice expansion
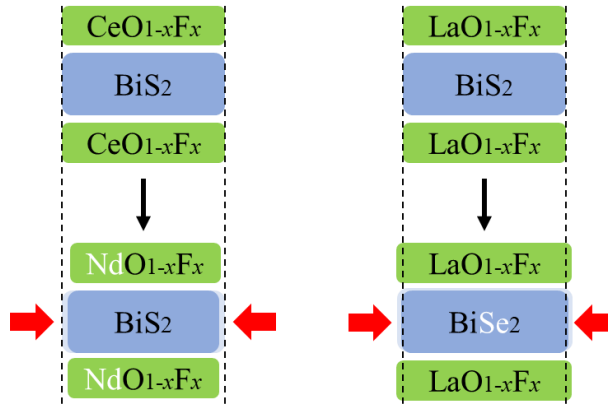


Fig. 11. Conceptual diagram of chemical pressure by elemental substitution.
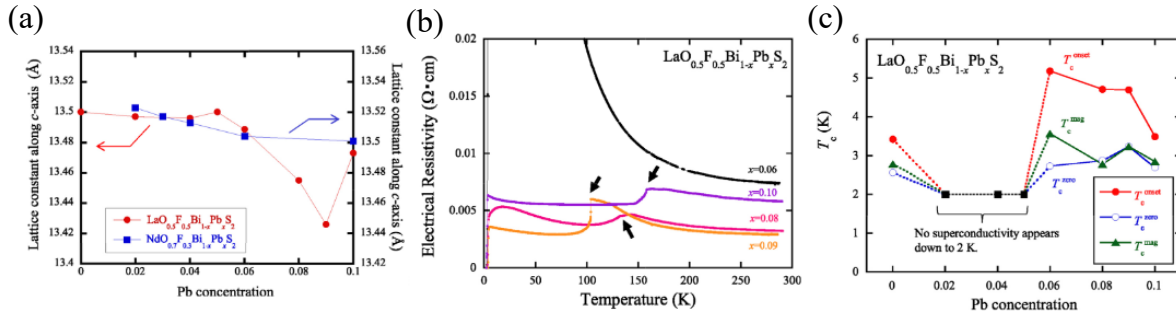


Fig. 12. ©2017 Elsevier Ltd. (Solid State Commun. 270, 17). (a) Lattice parameter along the $c$-axis for $LaO_{0.5}F_{0.5}Bi_{1-x}Pb_xS_2$ and $NdO_{0.7}F_{0.3}Bi_{1-x}Pb_xS_2$ (b) Temperature dependence of electrical resistivity for $LaO_{0.5}F_{0.5}Bi_{1-x}Pb_xS_2$ from 2 K to 300 K. (c) Pb concentration $x$ dependence of $T_c$ for $LaO_{0.5}F_{0.5}Bi_{1-x}Pb_xS_2$.

owing to Se substitution is smaller than expected. As a result, the density in the conduction plane increases, and CP occurs in the direction of the red arrow.

In addition to the CP, elemental substitutions have been suggested to change the crystal structure. In single crystal $LaO_{0.5}F_{0.5}BiS_2$, when the Bi in the conducting layer was partially replaced by Pb, a kink in the temperature dependence of the electrical resistivity was found to appear and superconducting properties were enhanced with only a few percent's Pb substitution as shown in Fig. 12 (b).[25] Because the lattice parameters change near this composition as shown in Fig. 12 (a), it has been pointed out that the substitution of Bi with Pb may have caused a structural change.[25] On the other hand, no such phenomenon has been observed in Pb substituted $NdO_{0.7}F_{0.3}BiS_2$.[22] Thus, it is expected that $LaO_{0.5}F_{0.5}BiS_2$, which includes the lanthanide element with the largest ionic radii, has potentially structural instability and tends to undergo a structural change which may lead the enhancement of superconducting property by elemental substitution.

## 3.2 Object of this chapter

As described above, $La(O,F)BiS_2$ has potentially structural instability, and it is suggested that the crystal structure can be changed by replacing Bi sites in the conduction layer with Pb, accompanied with an enhancement of $T_c$.

The objective of this study is to investigate the change in crystal structure and superconducting properties of $LaO_{0.5}F_{0.5}BiS_2$ when the Bi site is partially substituted with Sn, which belongs to the same group as Pb.

## 3.3 Experiments
## 3.3.1 Sample preparation and physical property measurement methods

Sn substituted $LaO_{0.5}F_{0.5}BiS_2$ was prepared by the flux method. The amount of F was fixed at 0.5 for all compositions and the nominal Sn value $x_n$ was varied from 0 to 0.18. All samples except $x_n = 0.18$ used $La_2S_3$, $Bi_2O_3$, $BiF_3$, $Bi_2S_3$, Bi and Sn as starting materials. $x_n = 0.18$ was prepared by the flux method. S was additionally used for the sample with $x_n = 0.18$ because the composition ratio of the preparation could not be achieved with the above starting material combination. The flux method required a flux to dissolve the material. 5:3 molar ratio CsCl and KCl were used for flux. The starting material and flux were vacuum sealed in quartz tube and heated in a furnace. The quartz tube was heated in the furnace to 900°C and then cool it slowly to 600°C to obtain a single crystal. Electrical resistivity measurements, magnetic susceptibility measurements, and X-ray diffraction measurements were performed. In the powder X-ray diffraction measurement, the polycrystals obtained by powdering the single crystal were used for the measurement.

## 3.3.2 Sample characterization

The Sn concentration introduced into the samples was measured using an electron probe micro analyzer (EPMA) which is equipped with wave dispersive spectroscopy

(WDS) instead of energy dispersive spectroscopy (EDS). This enables to quantify elemental abundances with higher resolution. The relation between the nominal ($x_n$) and the measured ($x$) Sn concentration are shown in Fig. 13 (a). The measured Sn concentration $x$ increases linearly with nominal Sn concentration $x_n$. However, the measured Sn concentration was found to be about half of the nominal Sn concentration: we found the relation $x = 0.445\, x_n$, which will be used in the following. Nominal and the obtained Sn concentrations are summarized in Fig. 13 (a).

The EPMA analysis of Bi is also shown in Fig. 13 (b). Bi concentration decreases with nominal Sn concentration as expected. However, the sum of Bi and Sn concentration does not equal to 1, indicating the existence of defects as shown in Table I.

Temperature dependence of the electrical resistance was measured down to 2.5 K using the 4-terminal method. Temperature dependence of the magnetic susceptibility was measured down to 2 K using MPMS (Quantum Design). We defined the
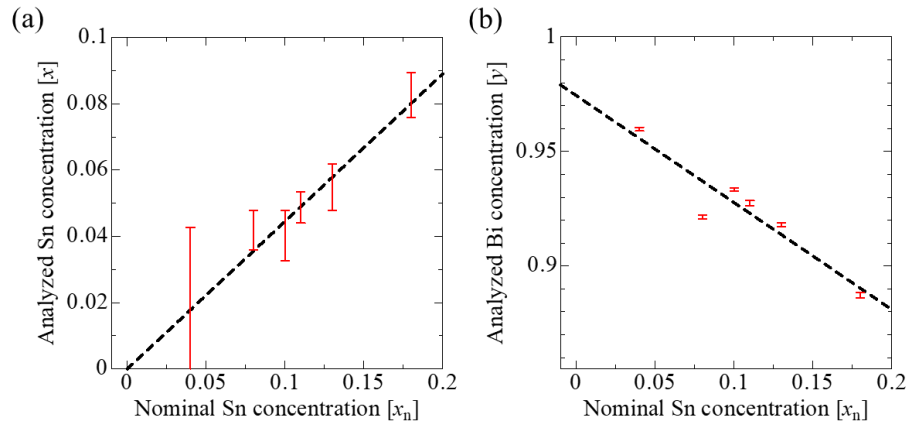


Fig. 13. (a) Nominal Sn concentration ($x_n$) versus Sn concentration ($x$) obtained by EPMA. The dotted line shown in the figure is the linear fitting: $x = 0.445\, x_n$. (b) Nominal Sn concentration versus Bi concentration obtained by EPMA. This figure reproduced from S. Kobayashi *et al.,* J. Phys. Soc. Jpn. 93, 024707 (2024) ©2024 The Physical Society of Japan (J. Phys. Soc. Jpn. 93, 024707).

Table I. The correspondence between the nominal Sn concentration $x_n$ and the Sn concentration $x$ obtained from the EPMA experiments. Sn concentrations were determined from the liner relation shown in Fig.13. Bi concentration obtained from EPMA experiments and the sum of Sn and Bi concentration are also shown. This table reproduced from S. Kobayashi *et al.,* J. Phys. Soc. Jpn. 93, 024707 (2024) ©2024 The Physical Society of Japan (J. Phys. Soc. Jpn. 93, 024707).

| Nominal Sn concentration ($x_n$) | 0 | 0.04 | 0.06 | 0.08 | 0.1 | 0.11 | 0.13 | 0.15 | 0.18 |
|---|---|---|---|---|---|---|---|---|---|
| Sn concentration ($x$) | 0 | 0.018 | 0.027 | 0.036 | 0.045 | 0.049 | 0.058 | 0.067 | 0.080 |
| Bi concentration | 0.974 | 0.955 | 0.946 | 0.937 | 0.927 | 0.923 | 0.913 | 0.904 | 0.890 |
| Total | 0.974 | 0.973 | 0.973 | 0.972 | 0.972 | 0.972 | 0.971 | 0.971 | 0.970 |

superconducting transition temperature as follows. For electrical resistivity measurements, $T_c^{onset}$ is defined as the temperature at which the electrical resistivity begins to decrease, and $T_c^{zero}$ is defined as the temperature at which the electrical resistivity becomes zero. For the magnetic susceptibility measurement, $T_c^{mag}$ is defined as the temperature at which the magnetic susceptibility begins to decrease.

## 3.3.3 Synchrotron X-ray measurement methods

Synchrotron radiation X-ray diffraction (S-XRD) measurements were performed at the synchrotron radiation facility SPring-8 for both single and polycrystalline crystals. S-XRD measurements on single crystals were performed at BL02B1.[26] Before the measurements at SPring-8, single crystals without twins were selected using a laboratory system XRD system. The sample sizes, temperatures, and wavelengths of the X-ray beams used in the S-XRD measurements are summarized in Table II. Wavelengths were calibrated with polycrystal $CeO_2$. In the structural analysis of $x = 0.018$ and $0.058$, Bi and Sn occupancy were fixed at the values obtained from EPMA measurements.

Many X-ray oscillation photographs were obtained by changing $\omega$ from $0°$ to $180°$ in every $0.1°$ at different $\theta$, $\chi$ and $\varphi$ on a four-axis diffractometer installed at BL02B1.

The sample temperature was cooled down to 100 K using the helium blowing device installed in beamline BL02B1. The CrysAlis pro (Rigaku) was used for diffraction peaks indexing and integration. Structural parameters were refined by the SHELXL program.[27] The crystal structure was illustrated using the VESTA program developed by Momma and Izumi.[28]

For X-ray diffraction (XRD) measurements of $x = 0.027$, 0.036, 0.049 and 0.080

Table II. The sample sizes, temperatures, and wavelengths of X-ray beams used in the S-XRD measurements. This table reproduced from S. Kobayashi *et al.,* J. Phys. Soc. Jpn. 93, 024707 (2024) ©2024 The Physical Society of Japan (J. Phys. Soc. Jpn. 93, 024707).

|  | $x = 0$ | | $x = 0.018$ | | $x = 0.058$ |
| --- | --- | --- | --- | --- | --- |
| Temperature (K) | 300 | 100 | 300 | 100 | 100 |
| Wavelength (Å) | 0.248624 | | 0.413172 | | 0.413172 |
| Sample size (μm³) | 50×50×15 | | 65×45×11 | | 62×45×11 |

polycrystals, beamline BL02B2 at the synchrotron facility SPring-8, Japan was used.[29–31] X-ray data profiles of the polycrystals were obtained using a MYTHEN diffractometer installed at BL02B2. In the measurements for polycrystals, X-ray beam with a wavelength of $\lambda = 0.495785$ Å was used. This wavelength was calibrated with the X-ray profile of polycrystal $CeO_2$. The sample temperature was cooled down to 100 K using the helium blowing device installed in beam line BL02B2. The EXPO2014 was used for diffraction profiles analysis, lattice parameters and phase ratio. [32]

## 3.4 Results

### 3.4.1 Result of electrical resistivity and magnetic susceptibility measurement
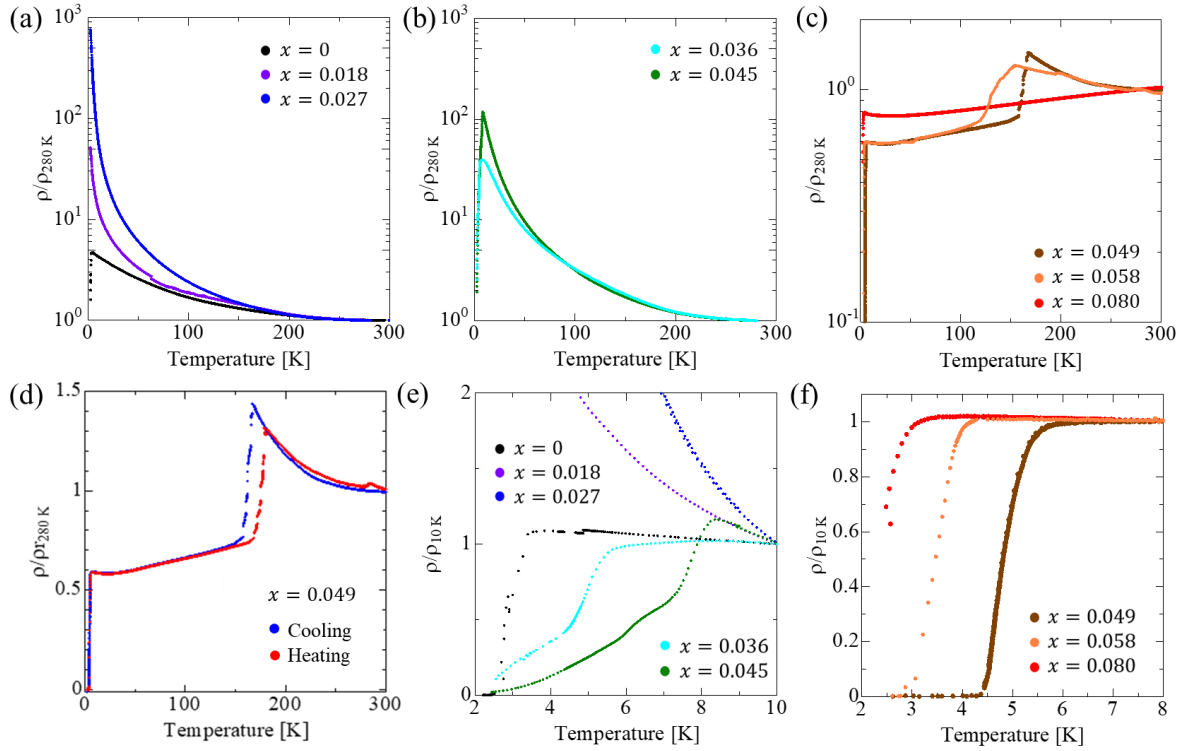


Fig. 14. Temperature dependence of the electrical resistivity for $LaO_{0.5}F_{0.5}Bi_{1-x}Sn_xS_2$. (a) $x$ = 0 - 0.027, (b) $x$ = 0.036 and 0.045, and (c) $x$ = 0.049 - 0.080 from 2 K to 280 K in a logarithmic scale. (d) Thermal hysteresis of the resistivity in $x$=0.049. (e) $x$ = 0 - 0.045 and (f) $x$ = 0.049 - 0.080 from 2 K to 10 K in a liner scale. This figure reproduced from S. Kobayashi *et al.,* J. Phys. Soc. Jpn. 93, 024707 (2024) ©2024 The Physical Society of Japan (J. Phys. Soc. Jpn. 93, 024707).

The temperature dependence of the electrical resistivity was measured for single crystals from $x$ = 0 to 0.080 and is shown in Figs. 14 (a), (b), and (c). As the Sn concentration is increased from $x$ = 0 to 0.027, the semiconducting behavior gradually becomes stronger, and the electrical resistivity at low temperatures is the highest at $x$ = 0.027, as shown in Fig. 14 (a). However, it decreases with further increases in Sn concentration as $x$ = 0.036 and 0.045 (Fig. 14 (b)).

The temperature dependence of the electrical resistivity of the samples with $x$ = 0.049 and 0.058 shows a different feature: A large jump is observed around 180 K as shown in Fig. 14 (c). In addition, the sample shows metallic temperature dependence below this temperature, whereas the temperature dependence of electrical resistivity shows semiconducting behavior above this temperature as well as below $x$ = 0.045.

We found that this large jump in the electrical resistivity in $x$=0.049 sample accompanied a thermal hysteresis as shown in Fig. 14 (d). This indicates that the

28

observed large jump corresponds to a first-order phase transition. This is the first observation of the large jump of electrical resistivity with the thermal hysteresis in $BiS_2$-system.

For further increase in $x$ ($x$ = 0.080), the temperature dependence of the electrical resistivity becomes metallic in the temperature range measured (2.5 K - 300 K).

Figure 14 (e) and (f) show the magnified data of Figs. 14 (a), (b), and (c) below 10 K. For the $x$ = 0 sample, $T_c^{onset}$ is 2.5 K as was reported previously. In contrast, no superconducting transition was observed down to 2 K for the $x$ = 0.018 and 0.027 samples.
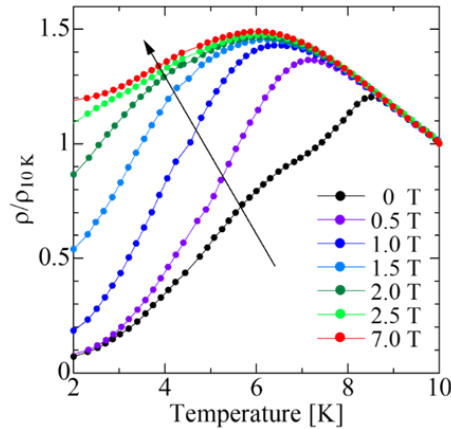


Fig. 15. Magnetic field dependence of the electrical resistivity for $x$ = 0.1 sample normalized at 10 K ($H$ // $c$ -axis). This figure reproduced from S. Kobayashi *et al.,* J. Phys. Soc. Jpn. 93, 024707 (2024) ©2024 The Physical Society of Japan (J. Phys. Soc. Jpn. 93, 024707).

However, with further Sn substitution, superconducting transition was again observed at $x$ = 0.036 and 0.045, with $T_c^{onset}$ at about 5 K and 8 K, respectively. $T_c^{zero}$ was about 2 K for both samples. At $x$ = 0.045, a kink can be seen at about 6 K. This seems to indicate the two-step transition.

To investigate whether these decreases in resistivity are owing to a superconducting transition, we measured the magnetic field dependence of the resistivity. In this measurement, a magnetic field was applied parallel to the $c$-axis. The results are shown in Fig. 15. The temperature at which the resistivity starts to decrease is reduced when the magnetic field applied. This indicates that the decrease in the resistivity is owing to the superconducting transition. The transition that exists at about 6 K under zero magnetic field disappears at 0.5 T. This indicates that the transition at about 6 K is also superconducting transition.

Figure 14 (f) shows the superconducting transition with further Sn substitution at $x$ = 0.049, 0.058, and 0.080. $T_c^{onset}$ of these samples are 5.5 K, 4.1 K, and 3.2 K for $x$ = 0.049, 0.058, and 0.080 respectively. These $T_c^{onset}$ are lower than those observed for $x$ = 0.036 and 0.045 samples. However, the $T_c^{zero}$ for $x$ = 0.049 and 0.058 samples become higher than those observed for low Sn concentration samples.
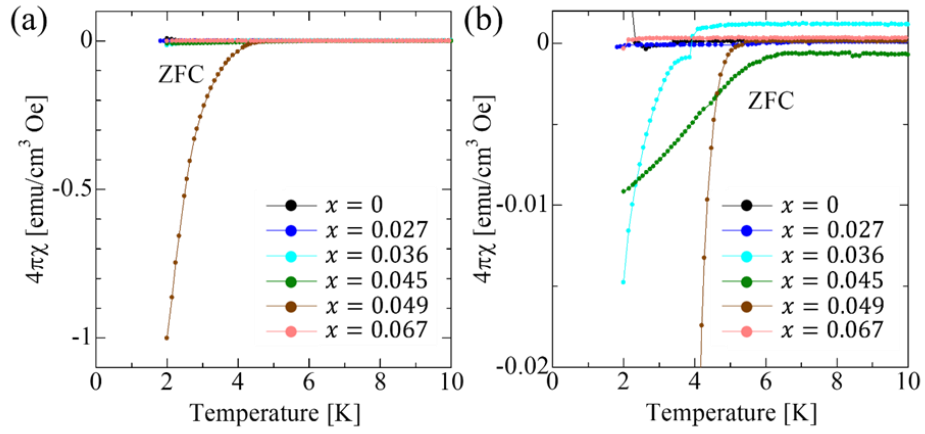
Fig. 16. Temperature dependence of the magnetic susceptibility for LaO$_{0.5}$F$_{0.5}$Bi$_{1-x}$Sn$_x$-S$_2$. ($H$ = 10 Oe // $c$-axis) (a) $x$ = 0 - 0.067 from 2 K to 10 K. (b) The magnified figure of (a). This figure reproduced from S. Kobayashi *et al.,* J. Phys. Soc. Jpn. 93, 024707 (2024) ©2024 The Physical Society of Japan (J. Phys. Soc. Jpn. 93, 024707).

   Next, the temperature dependence of the magnetic susceptibility was measured to investigate the superconducting transition. In this measurement, a magnetic field of 10 Oe was applied parallel to the $c$-axis. The results are shown in Fig. 16 (a) and (b). The $x$ = 0 sample has a superconducting volume fraction of less than 1% and no superconducting transition was observed in the magnetic susceptibility, which is consistent with the previous reports.[21,32]  This indicates the filamentary SC in $x$=0 sample. In magnetic susceptibility measurements, the superconducting transition was observed only at $x$ = 0.036, 0.045, and 0.049. For $x$ = 0.036 and 0.045, the superconducting volume fraction was about 1%. However, the superconducting volume fraction at $x$ = 0.049 is almost 100%, indicating the bulk SC. Note that the decrease in the susceptibility in the $x$ = 0.045 sample is observed at about 6 K. This temperature



Fig. 17. Sn concentration dependence of $T_c$. Measurements were performed down to 2 K. This figure reproduced from S. Kobayashi *et al.,* J. Phys. Soc. Jpn. 93, 024707 (2024) ©2024 The Physical Society of Japan (J. Phys. Soc. Jpn. 93, 024707).

30

corresponds to the temperature at which the kink appeared in the temperature dependence of resistivity (Fig. 14 (d)). This result suggests the existence of a two-step transition due to different superconducting volume fractions.
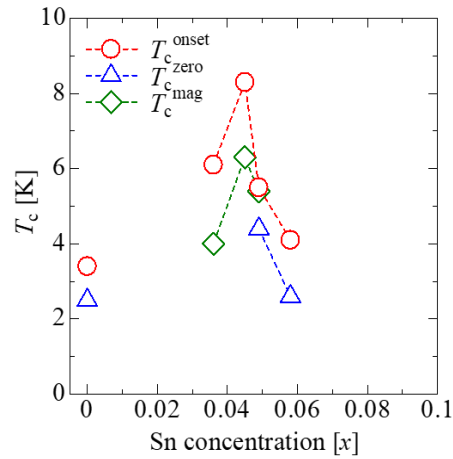
The Sn concentration dependence of $T_c$ obtained by electrical resistivity and magnetic susceptibility measurements is shown in Fig.17. We found that the increase in $T_c$ is not simply proportional to the increase in Sn concentration but is observed only in the vicinity of compositions showing large jumps in the temperature dependence of the resistivity (Fig. 14 (c)).

## 3.4.2 XRD measurements on $x = 0$ single crystal

Before the investigation of the structure of the Sn-substituted sample, the crystal structure for $x = 0$ sample was examined at 300 K and 100 K. A typical vibrational photograph at 100 K is shown in Fig. 19 (a). At 300 K and 100 K, all diffraction peaks followed the $P4/nmm$ diffraction conditions ($h + k = 2n$, when $l = 0$). This result is consistent with previous reports.[33] The refined fractional coordinate and thermal parameter at 100 K are shown in Table IV. The analysis converged well, yielding small

Table III. Results of crystal analysis of LaO$_{0.5}$F$_{0.5}$Bi$_{1-x}$Sn$_x$S$_2$ for $x = 0$ (300 K and 100 K), $x = 0.018$ (300 K and 100 K) and $x = 0.058$ (100 K). Reliability factors $R1$, $wR2$ and goodness-of-fit indicator $S$ are obtained from all reflections. This table reproduced from S. Kobayashi *et al.*, J. Phys. Soc. Jpn. 93, 024707 (2024) ©2024 The Physical Society of Japan (J. Phys. Soc. Jpn. 93, 024707).

| | $x = 0$ | | $x = 0.018$ | | $x = 0.058$ |
|---|---|---|---|---|---|
| Temperature (K) | 300 | 100 | 300 | 100 | 100 |
| Space group | $P4/nmm$ | | $P4/nmm$ | | $P2_1/m$ |
| | (tetragonal, SG:129) | | (tetragonal, SG:129) | | (monoclinic, SG:11) |
| $a$ (Å) | 4.07308(8) | 4.05983(3) | 4.08260(7) | 4.04692(5) | 4.05463(16) |
| $b$ (Å) | - | - | - | - | 4.06400(13) |
| $c$ (Å) | 13.4155(3) | 13.38183(15) | 13.5483(4) | 13.4374(2) | 13.0787(4) |
| $\beta$ (deg.) | 90 | 90 | 90 | 90 | 95.566(3) |
| $V$ (Å$^3$) | 222.563(10) | 220.562(4) | 225.817(10) | 220.072(6) | 214.495(13) |
| Number of unique reflections | 5832 | 5810 | 1246 | 1359 | 4017 |
| $R1$ | 0.0795 | 0.0577 | 0.0312 | 0.0459 | 0.0608 |
| $wR2$ | 0.2252 | 0.1668 | 0.0860 | 0.1118 | 0.1608 |
| $S$ | 1.201 | 1.075 | 1.141 | 1.229 | 1.096 |

$R1 = S| |F_o| - |F_c| | / S |F_o| [I > 2\sigma(I)]$ (all reflections), $wR2 = [S (w ( F_o^2 - F_c^2 )^2 ) / Sw (F_o^2)^2]^{1/2}$ (all reflections)

reliability factors (Table III). The obtained crystal structure at 100 K projected along the $a$-axis is shown in Fig. 18.

In the structural analysis of the $x = 0$ sample, the Bi site occupancy was parameterized. Such analysis still shows the presence of defects in Bi sites, which is consistent with the EPMA analysis shown in Table I. The presence of defects in Bi sites has been pointed out by Miura $et$ $al$.[33] Bi deficiencies in $R$(O,F)BiS$_2$ ($R$ = Nd, Ce) of 1-3% has been also reported.[34]
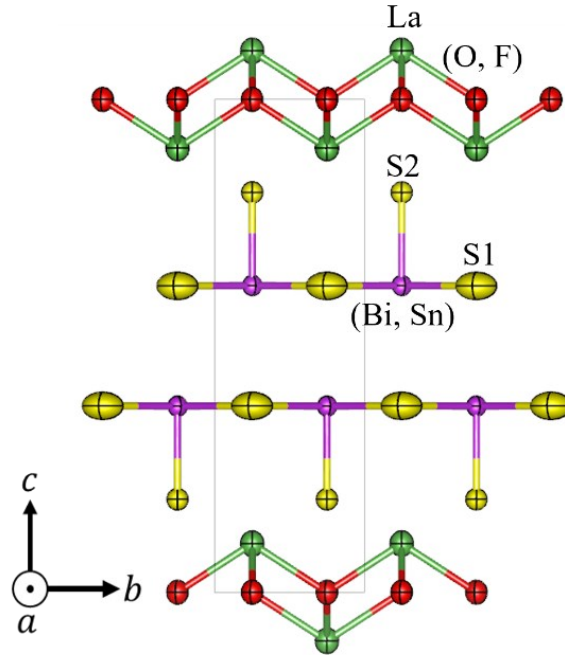


Fig. 18. Crystal structure of LaO$_{0.5}$F$_{0.5}$BiS$_2$ at 100 K projected along the $a$-axis. Each ion is shown with anisotropic thermal ellipsoids at 100 K. The probability of anisotropic thermal ellipsoids is 99%. This figure reproduced from S. Kobayashi $et$ $al$., J. Phys. Soc. Jpn. 93, 024707 (2024) ©2024 The Physical Society of Japan (J. Phys. Soc. Jpn. 93, 024707).

Table IV. Refined atomic coordinates ($x$, $y$, $z$), isotropic thermal parameters $B_{eq}$ and anisotropic thermal parameters $U_{nm}$ for $x = 0$ sample at 300 K and 100 K with space group $P4/nmm$. The temperature factor is expressed as $\exp(-2\pi^2(a^{*2}U_{11}h^2 + b^{*2}U_{22}k^2 + c^{*2}U_{33}l^2 + 2a^*b^*U_{12}hk + 2b^*c^*U_{31}hl + 2c^*a^*U_{23}lk)$. This table reproduced from S. Kobayashi *et al.,* J. Phys. Soc. Jpn. 93, 024707 (2024) ©2024 The Physical Society of Japan (J. Phys. Soc. Jpn. 93, 024707).

300 K

| Atom | Site | $x$ | $y$ | $z$ | $B_{eq}$ (Å$^2$) | Occ. |
|---|---|---|---|---|---|---|
| La | 2c | 1/4 | 1/4 | 0.09865(2) | 0.01310(3) | 1 |
| Bi | 2c | 1/4 | 1/4 | 0.62294(2) | 0.01422(3) | 0.946(2) |
| O | 2a | 3/4 | 1/4 | 0 | 0.0119(2) | 0.32(13) |
| F | 2a | 3/4 | 1/4 | 0 | 0.0119(2) | 0.68 |
| S1 | 2c | 1/4 | 1/4 | 0.3761(3) | 0.0292(5) | 1 |
| S2 | 2c | 1/4 | 1/4 | 0.81233(9) | 0.01232(11) | 1 |

| Atom | $U_{11}$ (Å$^2$) | $U_{22}$ (Å$^2$) | $U_{33}$ (Å$^2$) | $U_{12}$ (Å$^2$) | $U_{23}$ (Å$^2$) | $U_{31}$ (Å$^2$) |
|---|---|---|---|---|---|---|
| La | 0.01187(3) | 0.01187(3) | 0.01555(6) | 0 | 0 | 0 |
| Bi | 0.01517(4) | 0.01517(4) | 0.01232(4) | 0 | 0 | 0 |
| O | 0.0102(3) | 0.0102(3) | 0.0153(6) | 0 | 0 | 0 |
| F | 0.0102 | 0.0102 | 0.0153 | 0 | 0 | 0 |
| S1 | 0.0266(6) | 0.0266(6) | 0.0344(14) | 0 | 0 | 0 |
| S2 | 0.01230(15) | 0.01230(15) | 0.0124(2) | 0 | 0 | 0 |

100 K

| Atom | Site | $x$ | $y$ | $z$ | $B_{eq}$ (Å$^2$) | Occ. |
|---|---|---|---|---|---|---|
| La | 2c | 1/4 | 1/4 | 0.09861(2) | 0.00905(2) | 1 |
| Bi | 2c | 1/4 | 1/4 | 0.62245(2) | 0.00650(1) | 0.946(2) |
| O | 2a | 3/4 | 1/4 | 0 | 0.00803(18) | 0.32(13) |
| F | 2a | 3/4 | 1/4 | 0 | 0.00803 | 0.68 |
| S1 | 2c | 1/4 | 1/4 | 0.37829(16) | 0.0224(5) | 1 |
| S2 | 2c | 1/4 | 1/4 | 0.81133(7) | 0.00708(7) | 1 |

| Atom | $U_{11}$ (Å$^2$) | $U_{22}$ (Å$^2$) | $U_{33}$ (Å$^2$) | $U_{12}$ (Å$^2$) | $U_{23}$ (Å$^2$) | $U_{31}$ (Å$^2$) |
|---|---|---|---|---|---|---|
| La | 0.00844(3) | 0.00844(3) | 0.01027(4) | 0 | 0 | 0 |
| Bi | 0.00651(2) | 0.00651(2) | 0.00650(2) | 0 | 0 | 0 |
| O | 0.0075(2) | 0.0075(2) | 0.0091(4) | 0 | 0 | 0 |
| F | 0.0075 | 0.0075 | 0.0091 | 0 | 0 | 0 |
| S1 | 0.0276(7) | 0.0276(7) | 0.0118(5) | 0 | 0 | 0 |
| S2 | 0.00702(10) | 0.00702(10) | 0.00718(16) | 0 | 0 | 0 |

To reduce the parameters, we restricted $B_{eq}(O) = B_{eq}(F)$, $U_{nm}(O) = U_{nm}(F)$, xyz(O) = xyz(F), and occupancy(O) + occupancy(F) = 1.

## 3.4.3 XRD measurements on $x = 0.018$ single crystal

The crystal structure of $x = 0.018$ sample was examined at 300 K and 100 K. All diffraction peaks followed the $P4/nmm$ diffraction condition ($h + k = 2n$, when $l = 0$) at 300 K and 100 K as in $x=0$ sample. This result is consistent that both samples show

33

the similar semiconducting temperature dependence of the electrical resistivity. The structural analysis results at both 300 K and 100 K, and the refined fractional coordinated and thermal parameters at 100 K are summarized in Table III and Table V, respectively.

Table V. Refined atomic coordinates ($x$, $y$, $z$), isotropic thermal parameters $B_{eq}$, and anisotropic thermal parameters $U_{nm}$ for $x = 0.018$ sample at 100 K with space group $P4/nmm$. The temperature factor $U_{nm}$ is expressed as $\exp(-2\pi^2(a^{*2}U_{11}h^2 + b^{*2}U_{22}k^2 + c^{*2}U_{33}l^2 + 2a^*b^*U_{12}hk + 2b^*c^*U_{31}hl + 2c^*a^*U_{23}lk))$. This table reproduced from S. Kobayashi *et al.,* J. Phys. Soc. Jpn. 93, 024707 (2024) ©2024 The Physical Society of Japan (J. Phys. Soc. Jpn. 93, 024707).

100 K

| Atom | Site | $x$ | $y$ | $z$ | $B_{eq}$ (Å) | Occ. |
|---|---|---|---|---|---|---|
| La | 2c | 1/4 | 1/4 | 0.09770(3) | 0.01257(5) | 1 |
| Bi | 2c | 1/4 | 1/4 | 0.62381(2) | 0.01078(4) | 0.955 |
| Sn | 2c | 1/4 | 1/4 | 0.62381 | 0.01078 | 0.018 |
| O | 2a | 3/4 | 1/4 | 0 | 0.0122(5) | 0.59(14) |
| F | 2a | 3/4 | 1/4 | 0 | 0.0122 | 0.41 |
| S1 | 2c | 1/4 | 1/4 | 0.3785(2) | 0.0271(6) | 1 |
| S2 | 2c | 1/4 | 1/4 | 0.81129(12) | 0.01125(17) | 1 |

| Atom | $U_{11}$ (Å) | $U_{22}$ (Å) | $U_{33}$ (Å) | $U_{12}$ (Å) | $U_{23}$ (Å) | $U_{31}$ (Å) |
|---|---|---|---|---|---|---|
| La | 0.01161(7) | 0.01161(7) | 0.01448(11) | 0 | 0 | 0 |
| Bi | 0.01034(5) | 0.01034(5) | 0.01167(7) | 0 | 0 | 0 |
| Sn | 0.01034 | 0.01034 | 0.01167 | 0 | 0 | 0 |
| O | 0.0112(6) | 0.0112(6) | 0.0141(10) | 0 | 0 | 0 |
| F | 0.0112 | 0.0112 | 0.0141 | 0 | 0 | 0 |
| S1 | 0.0313(9) | 0.0313(9) | 0.0187(8) | 0 | 0 | 0 |
| S2 | 0.0109(2) | 0.0109(2) | 0.0119(4) | 0 | 0 | 0 |

To reduce the parameters, we restricted $B_{eq}$(O) = $B_{eq}$(F), $U_{nm}$(O) = $U_{nm}$(F), xyz(O) = xyz(F), and occupancy(O) + occupancy(F) = 1. Additionally, we restricted $B_{eq}$(Bi) = $B_{eq}$(Sn), $U_{nm}$(Bi) = $U_{nm}$(Sn), xyz(Bi) = xyz(Sn). Occupancies of Bi and Sn were fixed with the value of Table I.

## 3.4.4 XRD measurements on $x = 0.058$ single crystal

The sample at $x = 0.058$ showed the anomaly in the temperature dependence of the electrical resistivity as shown in Fig. 14 (c). In this section, we discuss the crystal structure of this sample. Figure 19 (b) shows X-ray oscillation photographs of ($h\,k\,0$) planes at 300 K. The observed diffractions do not fully satisfy the $P4/nmm$ reflection law: New weak reflections, which were not observed for $x = 0$ sample appeared. Specifically, there appeared reflections such as (3 2 0) or (3 4 0) which do not satisfy $h + k = 2n$. These reflections may come from the newly appeared structure.

Next, we observed the oscillation photograph on ($h\,k\,l$) ($l \neq 0$) plane (Fig. 19 (c)). On ($h\,k\,4$) plane, four reflections appeared surrounding the one that can be indexed as $P4/nmm$. These four reflections could not be explained by assuming $P4/nmm$ symmetry. Furthermore, any symmetry could not explain both the center and the four

34

surrounding reflections at the same time. Thus, at 300 K, it is thought that the crystal is composed of the mixture of *P*4/*nmm* and a new phase. Because four reflections surrounding the center one show fourfold symmetry, it seems that the coexisting new phase has monoclinic symmetry, which has four kinds of monoclinic domains.
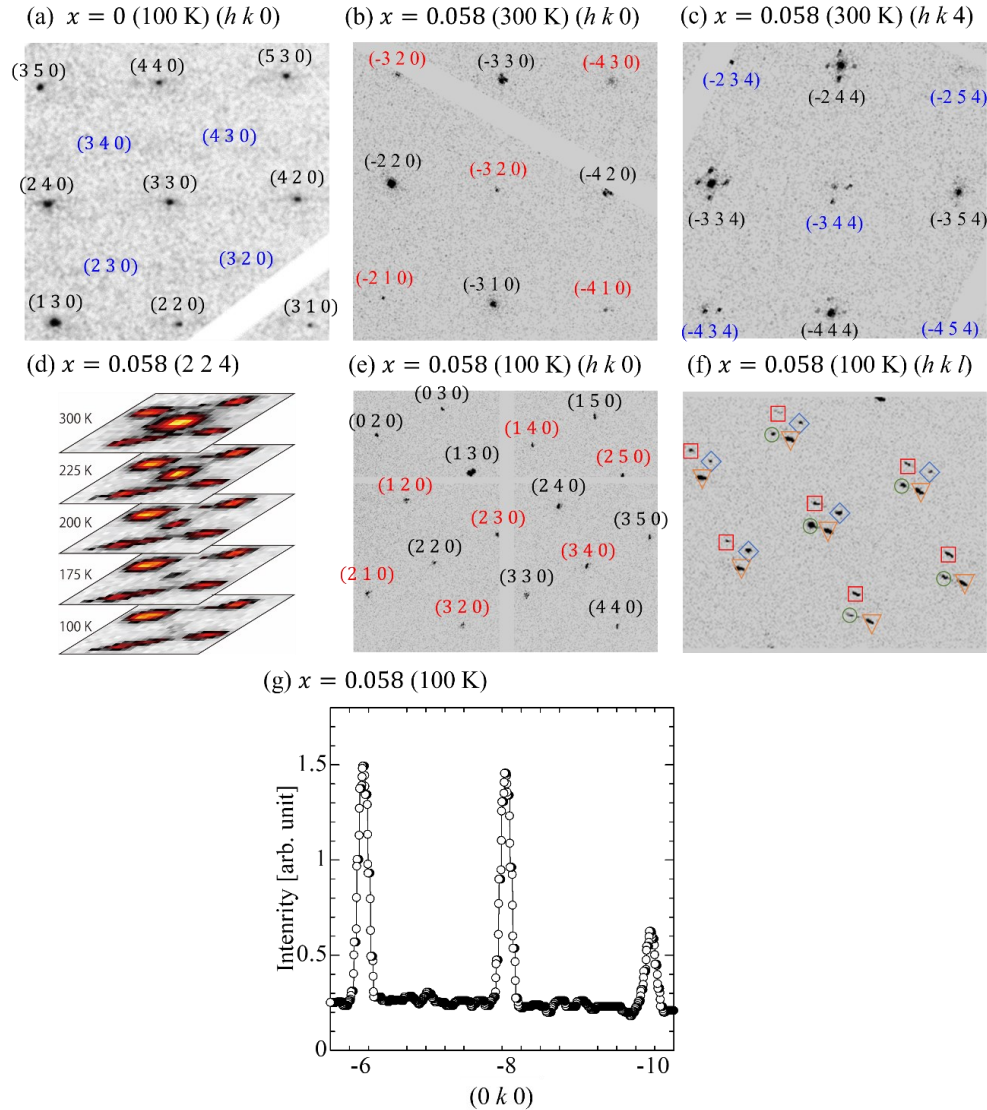


Fig. 19. X-ray oscillation photographs of $x$ = 0 and 0.058 sample. (a) ($h\,k\,0$) plane of $x$ = 0 sample at 100 K. Reflections with $h + k = 2n$ condition (shown in black) were clearly observed. While reflections with $h + k \neq 2n$ condition (shown in blue) were not seen. (b) ($h\,k\,0$) plane of $x$ = 0.058 sample at 300 K. Reflections with both $h + k = 2n$ (shown in black) and $h + k \neq 2n$ (shown in red) condition were observed. (c) ($h\,k\,4$) plane of $x$ = 0.058 sample at 300 K. (d) The temperature dependence of the reflections of $x$ = 0.058 sample near (2 2 5) reflection. (e) ($h\,k\,0$) plane of $x$ = 0.058 sample at 100 K. Reflections with both $h + k = 2n$ (shown in black) and $h + k \neq 2n$ (shown in red) condition were observed. (f) ($h\,k\,l$) plane of $x$ = 0.058 sample at 100 K. (g) (0 $k$ 0) line profile of $x$ = 0.058 sample at 100 K. This figure reproduced from S. Kobayashi *et al.,* J. Phys. Soc. Jpn. 93, 024707 (2024) ©2024 The Physical Society of Japan (J. Phys. Soc. Jpn. 93, 024707).

35

In $x = 0.058$ sample, electrical resistivity anomaly was observed around 180 K. Thus, we measured the temperature dependence of the reflection from 300 K to 100 K across the temperature at which the resistance anomaly was observed. Fig. 19 (d) shows the temperature dependence near $(2\,2\,4)$ reflection. At 300 K, strong $(2\,2\,4)$ reflection and four reflections around $(2\,2\,4)$ reflection can be seen in Fig. 19 (d). As the temperature is lowered, the intensity of $(2\,2\,4)$ reflection gradually decreases and completely disappears at 100 K. In contrast, the intensity of the four surrounding reflections gradually increases with decreasing temperature. This result clearly indicates that the structure of the sample changes across the temperature at which the electrical resistivity showed the anomaly.

During the temperature change, the center reflection which can be indexed by $P4/nmm$ symmetry disappeared, and the surrounding four reflections which could be identified by a new monoclinic structure was enhanced. Thus, we interpreted the observed temperature change is corresponding to the structural change from the mixture of $P4/nmm$ symmetry phase and a new monoclinic phase at 300 K to the single new monoclinic phase at 100 K. In other words, $P4/nmm$ symmetry phase at 300 K underwent structural phase transition to the monoclinic phase with the temperature decrease, whereas the monoclinic phase at 300 K unchanged.

To clarify the crystal structure at 100 K, the structural analysis was performed. Figure 19 (e) and (f) show oscillation photographs of $(h\,k\,0)$ and $(h\,k\,l)$ planes at 100 K, respectively. The result on $(h\,k\,0)$ plane shows both $h + k = 2n$ and $h + k \neq 2n$ reflections. This indicates that the $n$-glide symmetry of $P4/nmm$ disappears at 100 K. In addition, as shown in Fig. 19 (g), $(0\,k\,0)$ line profile indicates that the reflections appear only at $k = 2n$. This implies the existence of $2_1$ helical axisymmetry around the $b$-axis. From these results, the possible space group at 100 K is limited to monoclinic $P2_1/m$ or $P2_1$.

Because $\beta \neq 90°$ in the monoclinic structure, the unit cell of $P4/nmm$ (tetragonal) before the structural change could be tilted along four directions: $a$ (tetragonal), $-a$ (tetragonal), $b$ (tetragonal), and $-b$ (tetragonal). Thus, there could be four monoclinic domains, and the $(h\,k\,l)(l \neq 0)$ reflection splits into four reflections. Because $(h\,k\,0)$ reflection shown in Fig. 19 (e) does not have the component along the tilted $c$-axis, the reflection does not split.

To determine the symmetry, structural analysis considering the existence of four monoclinic domains was performed. The result showed that, assuming $P2_1/m$, the volume fractions of the four domains are $0.30345 : 0.28227 : 0.19797 : 0.21631$, which are realistic values with small reliability factors as shown in Table III. Thus, we concluded that the space group of the new monoclinic phase is $P2_1/m$. It is noted that this space group is the same as that appeared under the high-pressure or pristine LaOBiS$_2$.[21,35]

The structural analysis of one of the four domains of $P2_1/m$ is shown in Table VI. It should be noted that the value of $\beta$ is about 95.57°. This value is considerably larger than 90°. This is the reason why the clear splitting of reflections was observed in the

36

X-ray oscillation photographs of the $(h\,k\,l)(l \neq 0)$ plane shown in Fig. 19 (c), (d) and (f).

Table VI. Refined atomic coordinates $(x, y, z)$, isotropic thermal parameters $B_{eq}$, and anisotropic thermal parameters $U_{nm}$ for $x = 0.058$ sample at 100 K with space group $P2_1/m$. This table reproduced from S. Kobayashi *et al.,* J. Phys. Soc. Jpn. 93, 024707 (2024) ©2024 The Physical Society of Japan (J. Phys. Soc. Jpn. 93, 024707).

100 K

| Atom | Site | $x$ | $y$ | $z$ | $B_{eq}$ (Å$^2$) | Occ. |
|---|---|---|---|---|---|---|
| La | 2c | 0.21690(8) | 1/4 | 0.89961(3) | 0.01414(5) | 1 |
| Bi | 2c | 0.30557(5) | 1/4 | 0.38183(2) | 0.01341(4) | 0.913 |
| Sn | 2c | 0.30557 | 1/4 | 0.38183 | 0.01341 | 0.058 |
| O | 2a | 0.7487(9) | 1/4 | 0.0000(3) | 0.0137(4) | 0.50(16) |
| F | 2a | 0.7487 | 1/4 | 0.0000 | 0.0137 | 0.50 |
| S1 | 2c | 0.1215(4) | 1/4 | 0.63033(15) | 0.01612(19) | 1 |
| S2 | 2c | 0.3119(3) | 1/4 | 0.19171(11) | 0.01247(14) | 1 |

| Atom | $U_{11}$ (Å$^2$) | $U_{22}$ (Å$^2$) | $U_{33}$ (Å$^2$) | $U_{12}$ (Å$^2$) | $U_{23}$ (Å$^2$) | $U_{31}$ (Å$^2$) |
|---|---|---|---|---|---|---|
| La | 0.01352(9) | 0.01378(8) | 0.01528(9) | 0 | 0 | 0.00219(6) |
| Bi | 0.01342(6) | 0.01349(6) | 0.01333(6) | 0 | 0 | 0.00141(3) |
| Sn | 0.01342 | 0.01349 | 0.01333 | 0 | 0 | 0.00141 |
| O | 0.0127(9) | 0.0130(9) | 0.0156(10) | 0 | 0 | 0.0024(7) |
| F | 0.0127 | 0.0130 | 0.0156 | 0 | 0 | 0.0024 |
| S1 | 0.0137(4) | 0.0142(4) | 0.0205(5) | 0 | 0 | 0.0018(3) |
| S2 | 0.0117(3) | 0.0124(3) | 0.0135(4) | 0 | 0 | 0.0022(3) |

To reduce the parameters, we restricted $B_{eq}(O) = B_{eq}(F)$, $U_{nm}(O) = U_{nm}(F)$, xyz(O) = xyz(F), and occupancy(O) + occupancy(F) = 1. Additionally, we restricted $B_{eq}(Bi) = B_{eq}(Sn)$, $U_{nm}(Bi) = U_{nm}(Sn)$, xyz(Bi) = xyz(Sn). Occupancies of Bi and Sn were fixed with the value of Table I.

Figure 20 shows the drawings of the crystal structure obtained by the structural analysis at 100 K for the $x = 0.058$ sample, projected along the $a$-, $b$-, and $c$-axes. As shown in Figs. 20 (a) and (b), the S1 ions in the BiS$_2$ plane are uniformly displaced along the $a$- and $c$-axes. In adjacent BiS$_2$ layers, the displacement is in the opposite direction. The in-plane displacement along the $a$-axis is quite large, corresponding to the large value of $\beta = 95.57°$. Thus, as seen in Fig. 20 (c), two inequivalent Bi-S1 bonds form a two-dimensional zigzag chain in the BiS$_2$ plane in the diagonal direction.
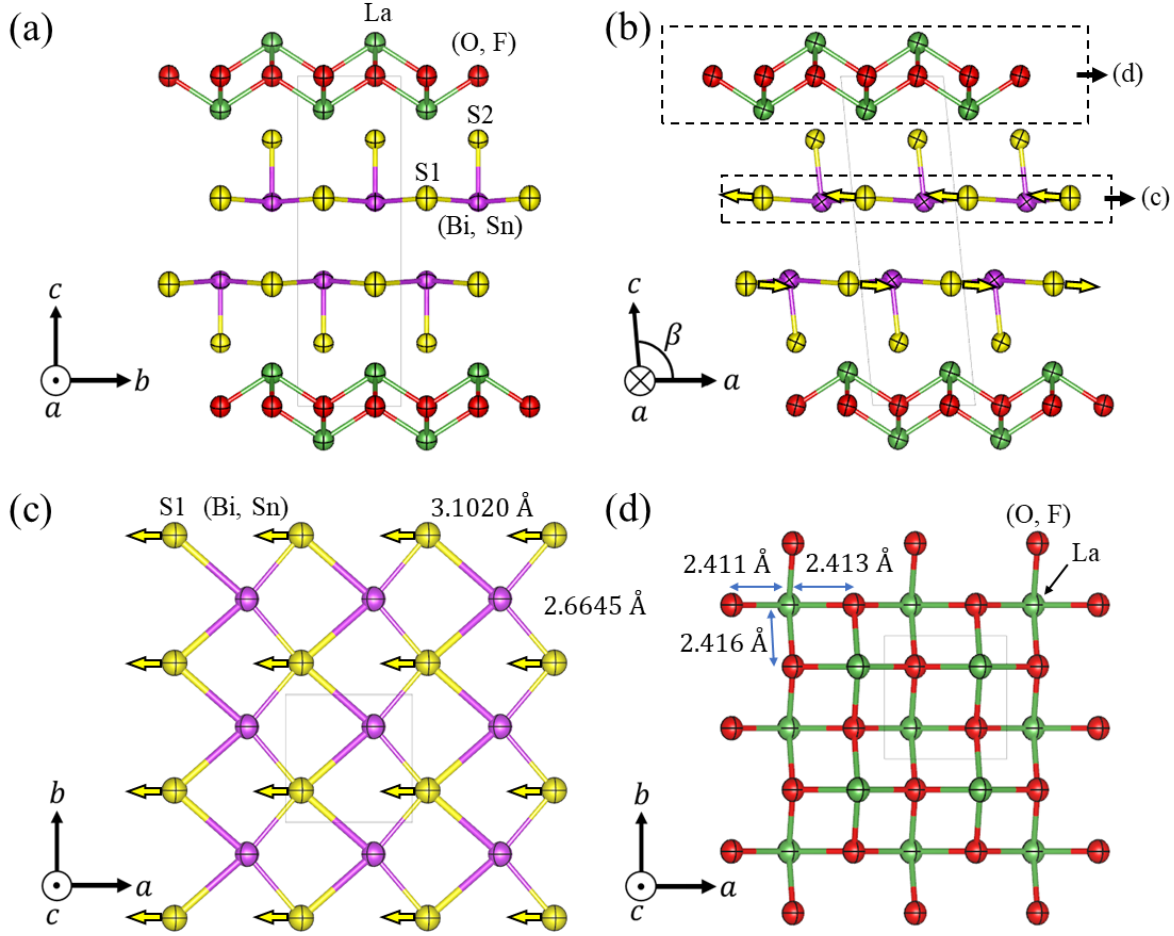
Fig. 20. (Color online) Crystal structure of $x = 0.058$ sample at 100 K projected along the (a) $a$-axis and (b) $b$-axis. (c) $BiS_2$ conducting layer projected along the $c$-axis. (d) La(O,F) blocking layer projected along the $c$-axis. Each ion is shown with anisotropic thermal ellipsoids at 100 K (the probability of anisotropic thermal ellipsoids is 99%). This figure reproduced from S. Kobayashi *et al.*, J. Phys. Soc. Jpn. 93, 024707 (2024) ©2024 The Physical Society of Japan (J. Phys. Soc. Jpn. 93, 024707).

## 3.4.5 Trend of the Volume fraction of $P4/nmm$ phase on amount of Sn

Because the crystal structure at 100 K of the $x = 0.058$ sample was determined to be $P2_1/m$, the coexisting monoclinic phase at 300 K is also $P2_1/m$. In this section, we evaluate the trend of the volume fraction of $P4/nmm$ and $P2_1/m$ phases which coexist at 300 K on amount of Sn. To investigate the trend, in addition to the single crystals, polycrystalline samples ($x = 0.027, 0.036, 0.049, 0.080$) were used for S-XRD measurements.

Figure 21 shows the trend of the volume fraction of the $P4/nmm$ phase versus Sn concentration. A volume fraction = 1 means that the entire crystal is in the $P4/nmm$
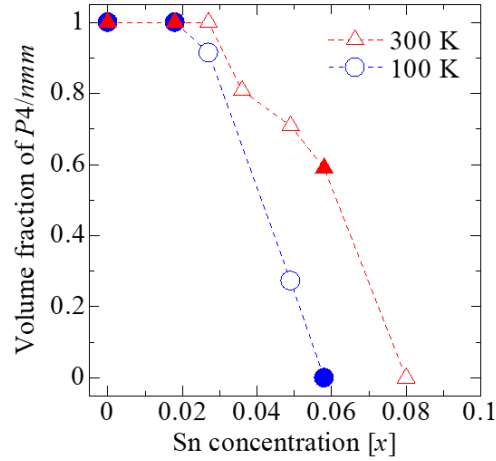
38

Fig. 21. Volume fraction of $P4/nmm$ phase verses Sn concentration. (Filled and open symbols show the results in the single crystals and the polycrystals, respectively.) In this figure, the reliability factors ($R_{wp}$, $R_B$) for each Sn contents of the polycrystal sample are as follows. The $x = 0.027$ is ($R_{wp}$, $R_B$) = (0.09282, 0.09893) (100 K) and (0.08873, 0.08535) (300 K). The $x = 0.036$ is ($R_{wp}$, $R_B$) = (0.09085, 0.11751) (300 K). The $x = 0.049$ is ($R_{wp}$, $R_B$) = (0.10745, 0.19522) (100 K) and (0.07958, 0.14516) (300 K). The $x = 0.080$ is ($R_{wp}$, $R_B$) = (0.11599, 0.10132) (300 K). This figure reproduced from S. Kobayashi *et al.,* J. Phys. Soc. Jpn. 93, 024707 (2024) ©2024 The Physical Society of Japan (J. Phys. Soc. Jpn. 93, 024707).

phase, while a volume fraction = 0 means that the entire crystal is in the $P2_1/m$ phase. Triangles and circles indicate volume fractions at 300 K and 100 K, respectively. The difference between triangles and circles indicates the volume fraction of the structural phase transition from the $P4/nmm$ phase to the $P2_1/m$ phase as the temperature is decreased. The anomaly in electrical resistivity seen in Fig. 14 (c) is observed at Sn concentrations where the difference of the volume fraction of $P4/nmm$ phase (difference between red and blue line in Fig. 21) is large. At such Sn concentrations, high $T_c$ is observed.
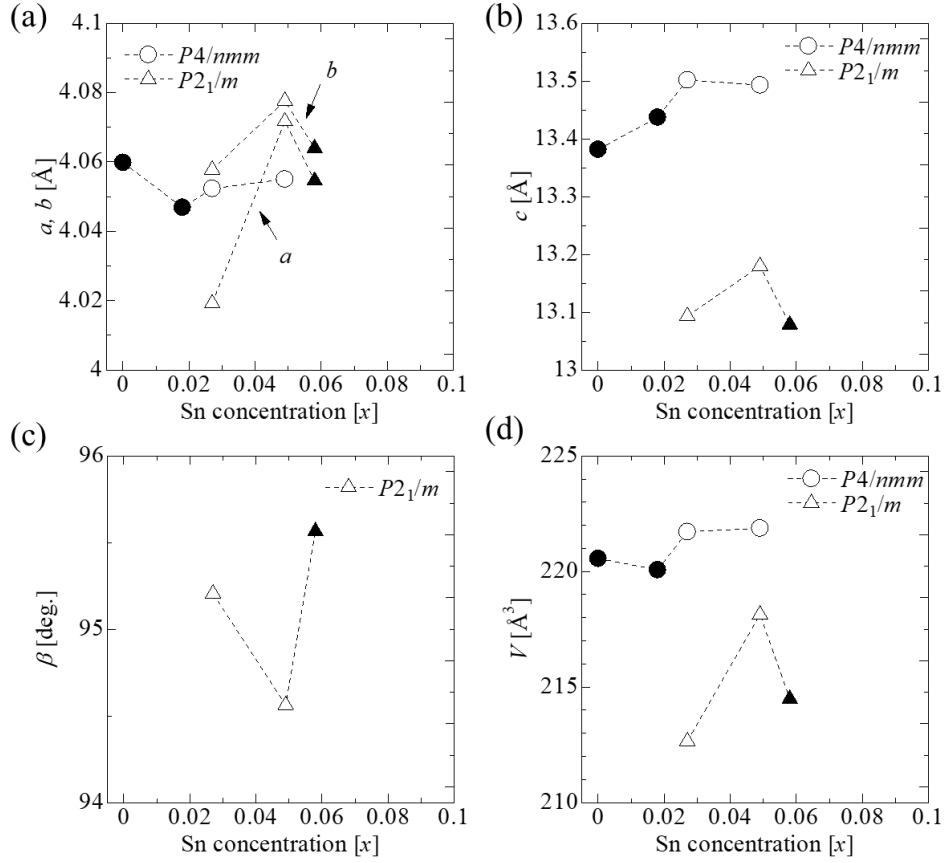
(a)

*P4/nmm*
*P2₁/m*

$a, b$ [Å]

$b$

$a$

Sn concentration [$x$]

(b)

*P4/nmm*
*P2₁/m*

$c$ [Å]

Sn concentration [$x$]

(c)

*P2₁/m*

$\beta$ [deg.]

Sn concentration [$x$]

(d)

*P4/nmm*
*P2₁/m*

$V$ [Å³]

Sn concentration [$x$]

Fig. 22. (a) - (e) Sn concentration dependence of the lattice parameters; $a$ and $b$, $c$, $\beta$, and $V$ at 100 K. (Filled and open symbols show the results in the single crystals and the polycrystals, respectively.) This figure reproduced from S. Kobayashi *et al.,* J. Phys. Soc. Jpn. 93, 024707 (2024) ©2024 The Physical Society of Japan (J. Phys. Soc. Jpn. 93, 024707).

The trends of the lattice constants with Sn concentration obtained from the structural analysis are also summarized in Figs. 22 (a)-(d).

## 3.5 Discussion

As shown in previous sections, the sample with $x \leq 0.018$ has a *P4/nmm* structure and the temperature dependence of electrical resistivity shows semiconducting behavior. With increasing Sn concentration, the structure changed from *P4/nmm* to *P2₁/m* with decreasing temperature, and the temperature dependence of resistivity became metallic behavior. This is the first report that clarified the existence of the structural phase transition in BiS₂-based superconductors under the ambient pressure and determined the resulting crystal structure.

A similar anomaly in the temperature dependence of resistivity is observed in the Pb-substituted LaO₀.₅F₀.₅BiS₂.[25] However, this anomaly is much smaller than in the Sn-substituted samples. Because the ionic radii of Bi, Pb, and Sn decrease in the order

of Bi > Pb > Sn, the structural instability causing the resistivity anomaly is considered to be enhanced by the decreasing ionic radii of the atoms substituting Bi sites. In $LaO_{0.5}F_{0.5}BiS_2$ ($P4/nmm$), the La-La distance in the blocking layer and the Bi(S1)-Bi(S1) distance in the conducting layer must be the same owing to symmetry requirements. Therefore, an elemental substitution in the conducting layer that change the average Bi(S1)-Bi(S1) distance would cause a mismatch with the blocking layer, leading the instability in the $P4/nmm$ structure. Thus, it is thought that substitution of Bi with an atom with a much smaller ionic radius than Pb induced the clear structural transition.

On the other hand, while Pb-substituted $LaO_{0.5}F_{0.5}BiS_2$ shows a small anomaly in the temperature dependence of resistivity, Pb-substituted $NdO_{0.7}F_{0.3}BiS_2$ even does not show that.[22] Because the ion radii of Nd is smaller than that of La, the blocking layer shrinks compared to $LaO_{0.5}F_{0.5}BiS_2$. When Bi is substituted with Pb, conducting layers also shrink. Thus, in Pb-substituted $NdO_{0.7}F_{0.3}BiS_2$, both blocking and conducting layers shrink, resulting smaller mismatch between the blocking and conducting layers. This may be the reason why Pb-substituted $NdO_{0.7}F_{0.3}BiS_2$ shows no anomalous temperature dependence of resistivity. This discussion also supports that the origin of the structural phase transition might be triggered by the mismatch between the blocking and conducting layers.

Among the $R$OBiS$_2$ family, La(O,F)BiS$_2$, which contains La with rather large ionic radius, particularly shows structural instability. In fact, monoclinic low-symmetry phase appears in $LaOBiS_2$ without F substitution, or $LaO_{0.5}F_{0.5}BiS_2$ under hydrostatic pressure.[36] Furthermore, the observed monoclinic phase was $P2_1/m$ symmetry in both cases. This suggests that $LaO_{0.5}F_{0.5}BiS_2$ with $P4/nmm$ structure is likely to transition to the $P2_1/m$ structure.

The Sn-substituted sample has the same $P2_1/m$ (monoclinic) symmetry as LaOBiS2 and hydrostatic $LaO_{0.5}F_{0.5}BiS_2$ as described above.[37] However, the $\beta$ values of the Sn-substituted sample, LaOBiS$_2$, and $LaO_{0.5}F_{0.5}BiS_2$ under hydrostatic pressure have different values of 95.57°, 90.12°, and 97.31°, respectively. Surprisingly, the $\beta$ of the Sn-substituted sample is close to the $\beta$ under hydrostatic pressure. In accordance with this change in $\beta$, the lattice constant along the $c$-axis decreases with increasing $\beta$, resulting in a 3.8 % decrease in unit cell volume for the Sn-substituted sample compared to $LaO_{0.5}F_{0.5}BiS_2$ under ambient pressure. This value is comparable to the 6.5 % decrease in unit cell volume observed under hydrostatic pressure of 4.0 GPa.

Next, the relationship between crystal structure and the temperature dependence of the electrical resistivity is discussed. The temperature dependence of the resistivity in $x = 0$ and $x = 0.018$ samples, which have $P4/nmm$ structure, show semiconducting temperature dependence. On $x = 0.049$ and $x = 0.058$ samples, which show structural phase transition at about 180 K, the temperature dependence shows semiconducting behavior above 180 K, and metallic behavior below 180 K. Structural analyses in the $x = 0.058$ sample shows that $P4/nmm$ and $P2_1/m$ phases coexist at 300 K, while at 100 K only $P2_1/m$ phase exists. Therefore, it is thought that $P4/nmm$ phase corresponds to the semiconducting behavior, while $P2_1/m$ phase corresponds to metallic behavior.

On the other hand, Nd(O,F)BiS$_2$ is reported to exhibit metallic-like temperature dependence of electrical resistivity despite its *P4/nmm* crystal structure.[37] This means that the difference between *P4/nmm* and *P2$_1$/m* does not necessarily explain the semiconducting and metallic behavior of the *R*OBiS$_2$ family. Rather, the differences may stem from disorders in *P4/nmm* crystal structure of La(O,F)BiS$_2$.

In line with above discussion, the change in the steep increase in electrical resistivity at low temperature shown in Fig. 14 (a) could be explained: With increasing Sn concentration form $x = 0$ up to $x = 0.027$, where the sample is *P4/nmm* single phase, the steep increase is enhanced. This enhancement is thought to stem from the increase in the disorder owing to Sn substitution. On the other hand, above $x = 0.027$, as shown in Fig. 14 (b), the steep increase is reduced. Looking at the volume fraction of *P4/nmm* phase shown in Fig. 21, above $x = 0.027$, the volume fraction of *P4/nmm* phase decreases and that of *P2$_1$/m* phase increases. Thus, the suppression of the steep increase in resistivity for $x = 0.036$ and $x = 0.045$ could be interpreted to stem from the appearance of the metallic *P2$_1$/m* phase.

Now let's move to the superconducting properties. Complex Sn concentration dependence of $T_c$ is summarized in Fig. 17. For $x = 0$ sample, a filamentary SC with $T_c$ ~ 2.5 K is observed, which is consistent with previous reports.[38] As the Sn concentration increases from $x = 0$, the superconducting transition disappears in the $x = 0.018$ and $x = 0.027$ samples. Because the $T_c$ of the *R*OBiS$_2$ family depends on the number of carriers[37,38], the change in $T_c$ may be owing to the change in the number of carriers owing to Sn substitution. A Core level spectroscopy measurement shows that the Sn valence at the Bi site is about +2, and the Sn substitution is a hole doping.[39] Therefore, this suppression of $T_c$ is interpreted to stem from the reduction of electron carrier owing to the Sn substitution.

When the Sn concentration is further increased, the superconducting transition appears again. This cannot be explained by a change in the number of carriers. Furthermore, near the Sn concentration where the structural phase transition occurs, superconducting properties such as $T_c$ and superconducting volume fraction are enhanced. Above the Sn concentration, $T_c$ and the superconducting volume fraction decrease again. This result suggests that the structural differences between *P4/nmm* and *P2$_1$/m* do not determine the superconducting properties. Therefore, the enhancement of superconducting properties is related to the structural phase transition itself.

There are several effects of the structural phase transition on the superconducting properties. One is the chemical pressure owing to the coexistence of *P4/nmm* and *P2$_1$/m* structures. Because of the different $\beta$ or the unit cell volume of both phases, coexistence possibly induce stronger chemical pressure than that for usual elemental substitution.

Another effect is the change in $U_{11}$ of S1 atom. In a previous report, it was pointed out that a decrease in $U_{11}$ and an increase in $U_{33}$ of the S1 atom is associated with an increase in $T_c$. In the present experiment, the $x = 0.058$ sample (Table VI) shows a

similar trend of decreasing $U_{11}$ and increasing $U_{33}$ compared to the pristine sample (Table IV), although the crystal structure is the $P2_1/m$ structure.

Because it is difficult to quantitatively analyze the concentration of O and F, even with EPMA analysis or synchrotron XRD measurements, F concentration, which affects the number of carriers, has not been discussed so far. F concentration may change from the nominal value when Sn concentration changes. However, the maximum $T_c$ of the Sn-substituted sample is about 8 K, which is much higher than 2.5 K for the unsubstituted sample. Therefore, it could be concluded that the improvement in superconducting properties is the effect of Sn substitution.

## 3.6 Conclusion

We found that partial substitution of Bi with Sn in $LaO_{0.5}F_{0.5}BiS_2$ induces a structural phase transition from the semiconducting $P4/nmm$ structure to the metallic $P2_1/m$ structure. The bulk superconductivity with $T_c$ of about 6 K is found to emerge near the composition at which the structural phase transition occurs. We also found that filamentary superconductivity with $T_c$ of about 8 K, which is nearly three times higher than that of the unsubstituted sample. Although the reason why a mere about 5 at% substitution leads the structural change is open question, this finding provides a new route to further increase in the superconducting transition temperature in this system.

# Chapter 4

## 4 Effects of lattice defects on physical properties in ZrTe₃

In this chapter, I will discuss the effect of defects on the charge density wave (CDW) in ZrTe$_3$ from STM/STS measurements. Because STM/STS measurements are surface observation, the complemental bulk information was investigated by synchrotron X-ray diffraction measurements.

## 4.1 Introduction

A quasi-one-dimensional material ZrTe$_3$ has TiS$_3$ structure (space group: $P2_1/m$) as shown in Fig. 23.[40] The triangular prism of ZrTe$_3$, which includes three inequivalent Te sites (labeled as Te(1), Te(2) and Te(3)), forms quasi-one-dimensional chains along the $b$-axis direction. The quasi-one-dimensional chains are stacked in the $a$-axis direction and form layers, which are stacked in the $c$-axis direction. Thus, ZrTe$_3$ is anisotropic both in-plane and inter-plane directions. In fact, the transport properties are reported to be highly anisotropic.[41]
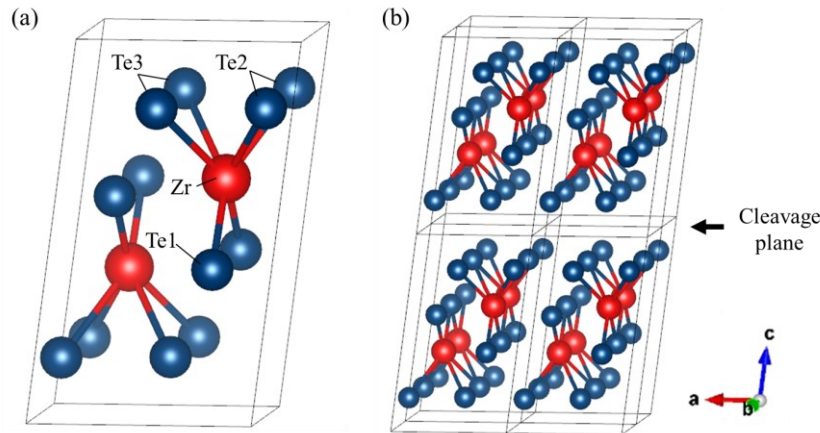


Fig. 23. Crystal structure of ZrTe$_3$.(a) unit cell of ZrTe$_3$ (b) $2 \times 2 \times 2$ unit cells

ZrTe$_3$ shows a CDW state below 63 K and the period of the CDW is about $14a_0 \times 3c_0$, appearing along $a$-axis and $c$-axis directions ($a_0$ and $c_0$ are lattice constants).[42] This CDW is considered as the Peierls-type CDW.[43]

In Fig. 24 (a), the angle-resolved photoemission spectroscopy (ARPES) intensity plot is overlaid with the Fermi surface (blue) obtained from a DFT calculation. The CDW is considered to be manifested by nesting of these one-dimensional fermi surfaces. Figure 24(b) show the temperature dependence of the ARPES spectra at D(E). The intensity around 200 mV is enhanced with decreasing temperature. This indicates the opening of the pseudo gap. The possible origin of the pseudo gap has not been clarified, but the fluctuation of the CDW has been thought to be a candidate.
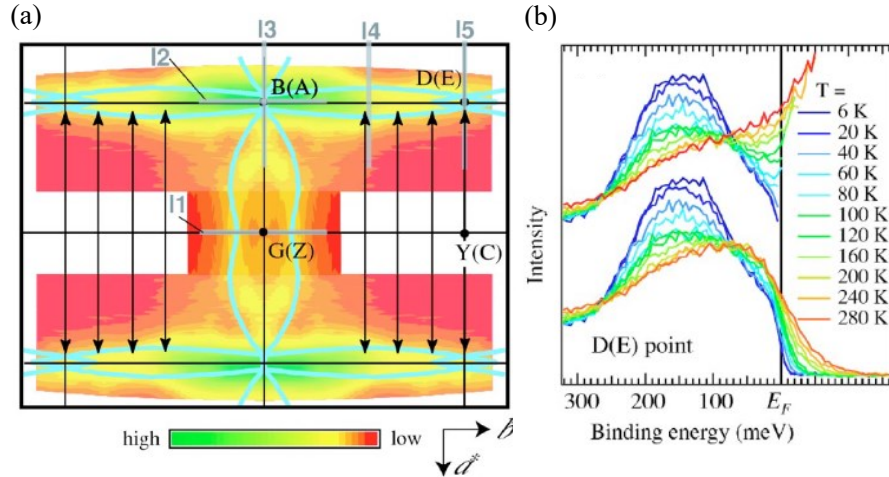
Fig. 24. ©2005 American Physical Society(Phys. Rev. B 71, 140504). Results of ARPES measurements in ZrTe$_3$. (a) ARPES intensity plot corresponding to experimental Fermi surface sheets, intersection of calculated FS sheets and BZ of ZrTe$_3$ with $k_z = 0$. Black arrows correspond to $a^*$ component of the CDW vector. (b) $T$-dependent (6–300 K) ARPES spectra.

In addition to the CDW state, ZrTe$_3$ shows superconductivity below 4 K. [44,45] Interestingly, superconductivity is filamentary and unidirectional. With the application of the pressure or substitution of Te for Se, bulk superconductivity appears with the suppression of the CDW order.[46] Furthermore, bulk superconductivity appeared in the samples prepared at higher temperature of 850℃ than conventionally used temperature of 650-700℃.[47] It is reported that this is caused by the appearance of two phases which have slightly different atomic positions of Zr and Te1. Thus, the structure of ZrTe$_3$ is rather flexible and this flexibility affects the superconducting properties.

In ZrTe$_3$, in addition to the disorder in atomic positions, the presence of atomic defects on the surface has been reported in STM measurements.[48] It is pointed out that defects strongly affect the CDW. The defect pin strongly the CDW near the CDW transition temperature ($T_{CDW}$), resulting the disordered CDW, whereas the pinning is weak well below $T_{CDW}$ and the coherent CDW is realized.

Although the pinning of the CDW by atomic defects is realized, it is thought that atomic defects is not so effective for pinning because the in-plane period of CDW in ZrTe$_3$ is 14$a_0$, which is quite large relative to the atomic defect size. Thus, additional effect which enhances the pinning is expected. In fact, near the atomic defects, streaks or stripe like contrast have been reported in STM experiments. [48]

On possible candidate of such effect is Friedel oscillation. Friedel oscillation arises from the scattering of the conduction electrons by a defect, which has the wave number of 2k$_F$. The possible development of Friedel oscillation in ZrTe$_3$ has been reported from soft x-ray diffraction measurement.[49] In this measurements near $T_{CDW}$, a strong and sharp CDW signal and a weak and broad signal with a component

close to the CDW component were observed. This weak and broad signal is considered to originate from Friedel oscillation. The trace of the weak broad signal remained above $T_{CDW}$, suggesting that CDW fluctuation may exist above $T_{CDW}$.

## 4.2 Object of this chapter

If Friedel oscillation is realized in $ZrTe_3$ and is responsible for the pinning, it can be expected to understand the phenomena which is different from those in ordinary pinning by atomic defects.

Furthermore, because STM is the surface experiment, the existence of the defects in the bulk, which is responsible to the soft X ray diffraction measurements, cannot be examined. Thus, the clarification of the existence of the defect in the bulk by the detailed structural analysis is needed. Although, composition analysis such as EDX or EPMA provides the information of the amount of the defects, in $ZrTe_3$, there are some Te sites as shown in Fig. 23 and some of them are not responsible for the CDW. Thus, to investigate the defects, the detailed structural analysis by diffraction which enables to determine the site dependent number of defects is needed.

Thus, to investigate the pinning of the CDW in $ZrTe_3$, we examined low temperature STM experiments. In addition, we performed synchrotron X ray diffraction experiments to analyze the atomic defects.

## 4.3 Experiments
## 4.3.1 Sample preparation and physical property measurement methods

Polycrystal $ZrTe_3$ used for Synchrotron X-ray measurements was prepared using a two-step solid phase reaction method to obtain uniform crystals. In the first step of synthesis, 1:3 ratio of Zr (99.9%) and Te (99.999%) were heated in the evacuated quart tube at 800°C for 48 h to complete the reaction, and finally, ice quenched. In the second step of synthesis, $ZrTe_3$ obtained in the first step was pelletized to obtain homogeneous crystals. The synthesis was carried out at 650°C for 72 h. Finally, an ice quench was performed. The pellets were then powdered again and sealed in a capillary for synchrotron X-ray measurements.

ZrTe$_3$ single crystals used for STM measurements were prepared using the chemical vapor transport (CVT) method. $ZrTe_3$ polycrystals were used as the starting material. $ZrTe_3$ polycrystals were prepared as described above. The polycrystals and iodine (5 mg/cc) are sealed in the evacuated quartz tube and heated at a temperature gradient of 750°C/650°C for 2 weeks. Single crystals grown in different temperature ranges have different $T_{CDW}$.[47,50] Therefore, to obtain crystals with the same $T_{CDW}$, obtained single were annealed at 650°C, and finally ice quench was performed.

To evaluate the $ZrTe_3$ single crystal prepared by this method, we measured the temperature dependence of electrical resistivity using the four-terminal method. Figure 25 (a) shows the temperature dependence of the electrical resistivity along the *a*-axis. Clear hump owing to the CDW transition is observed around 60 K. Figure 25 (b) shows the numerical differentiation of the temperature dependence of electrical
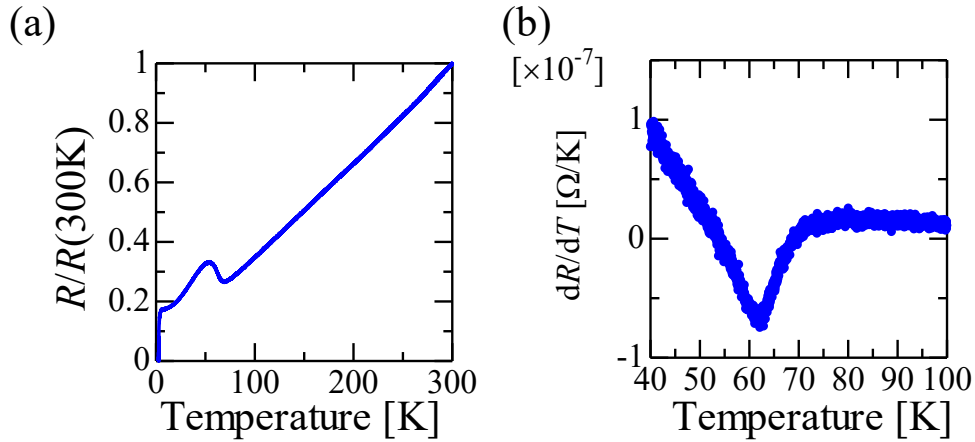
(a)

(b)

Fig. 25. Temperature dependence of the electrical resistance in ZrTe$_3$ along the a-axis. (a) Temperature dependence of the electrical resistance normalized at 300 K. (b) Numerical differentiation of (a). © [2023] The Authors(S. Kobayashi *et al*). Originally published in JPS Conference Proceedings 38, 011053 (2023)], [Decoherence in CDW above CDW Transition Temperature in ZrTe3], [DOI: 10.7566/JPSCP.38.011053].

resistivity shown in Fig. 25 (a). The $dR/dT$ begins to decrease from around 70 K, and reaches its minimum value at 62 K. Because the minimum value of $dR/dT$ is defined as as the CDW transition temperature, CDW transition temperature is 62 K and the transition begins gradually around 70 K. Therefore, 80 K, one of the temperatures at which STM measurements were performed, is above the temperature at which the CDW transition begins.

## 4.3.2 Synchrotron X-ray measurement method

Synchrotron X-ray diffraction (S-XRD) measurements of ZrTe$_3$ was carried out at beamline BL02B2 at the synchrotron facility SPring-8 Japan.[29–31] X-ray data profile of the polycrystal was obtained using a MYTHEN diffractometer installed at

Table VII. Measurements conditions and results of crystal analysis of ZrTe$_3$.

| Annealing Temperature (℃) | 650 |
|---|---|
| Temperature (K) | 300 |
| Sample type | polycrystal |
| Wavelength (Å) | 0.4959 |
| 2 θ(deg.) range | 2.100 - 78.216 |
| a  (Å) | 5.89224(10) |
| b (Å) | 3.92336(6) |
| c (Å) | 10.10706(18) |
| β(deg.) | 98.1575(17) |

BL02B2. The wavelength was calibrated with the X-ray profile of polycrystal $CeO_2$. The Rietan-FP was used for diffraction profile analysis.[52]

Because prepared $ZrTe_3$ polycrystals contains $ZrTe_5$ polycrystals, Rietveld analysis was performed with the assumption that both $ZrTe_3$ and $ZrTe_5$ exist. The measurement conditions are shown in Table VII. The crystal structure was illustrated using the VESTA program developed by Momma and Izumi.[28]

### 4.3.3 STM/STS measurement method

The STM/STS measurements were performed using a laboratory made STM. Measurement temperatures were 4.2 K and 80 K. The clean surface was prepared by cleavage at the measurement temperatures in vacuum.

## 4.4 Results
## 4.4.1 STM/STS measurements

Figure 26 (a) shows the spatially averaged tunneling spectra at 4.2 K and 80 K. At both temperatures, two peaks at about +150 mV and -170 mV were observed (indicated by red arrows). These peaks are consistent with the pseudo gap reported in the ARPES measurements.[52]

Figure 26 (b) shows the spectra in ±50 mV range. A dip can be seen around +20 mV at 4.2 K, indicated by the red arrow, whereas at 80 K such dip cannot be seen. Fig. 26 (c) is $d^2I/dV^2$ of the spectra shown in Fig. 26 (b). The anomaly at 20 mV at 4.2 K can be seen clearly. Because the dip was observed only below $T_{CDW}$, it is thought that the dip relates to the CDW gap.

Figure 27 (a) and (b) show STM images obtained at 4.2 K and 80 K, respectively. At both temperatures, many white streaks (strip-like structures) can be seen running along the $c$-axis. The stripe structure was confirmed to have a point defect at its center as shown in Fig. 27 (inset) . Thus, the stripe structure is thought to be caused by the point defect.
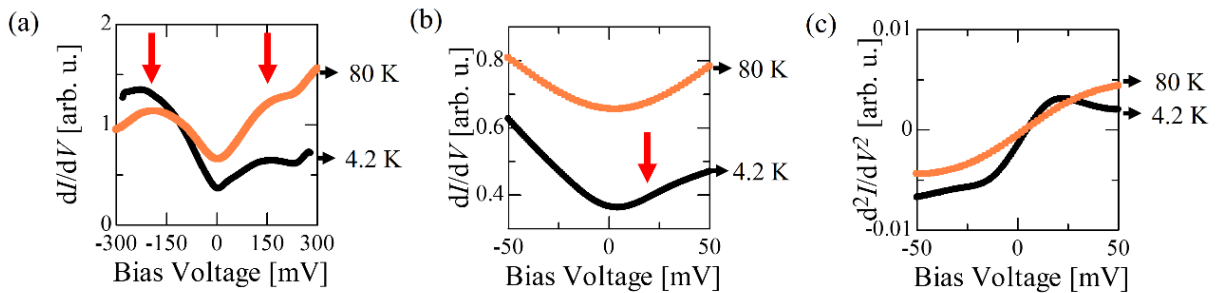


Fig. 26. (a) Spatially averaged tunnel spectra $dI/dV$ at 4.2 K and 80 K ($V_{Bias} = 100$ mV, $I_t = 100$ pA). These spectra were normalized at $V_{Bias} = -100$ mV. (b) $dI/dV$ in the range from -50 mV to +50 mV. (c) Numerical differentiation of (b). © [2023] The Authors(S. Kobayashi *et al*). Originally published in JPS Conference Proceedings 38, 011053 (2023)], [Decoherence in CDW above CDW Transition Temperature in $ZrTe_3$], [DOI: 10.7566/JPSCP.38.011053].

At 4.2 K, the observed CDW modulation is rather regular, indicating the existence of the long-range order, despite the existence of the defects. This indicates that defect pinning is weak at this temperature. Figure 27 (c) shows the fast Fourier transform (FFT) image of Fig. 27 (a). Bragg peaks in the $a$- and $b$-axis directions are shown as triangles and inverse triangles, respectively. The inset is a magnified image of the center of the FFT image, which shows sharp peaks only in the $a$-axis direction. These peaks correspond to the CDW with the period of $14a_0$, where $a_0$ is the lattice constant. Sharp peaks indicate regular CDW.

STM image at 80 K as shown in Fig. 27 (b) showed quite different aspect from that at 4.2 K as shown in Fig. 27 (b). A stripe-like contrast appearing in the vicinity of the defects and a faint spatial modulation with poor periodicity were observed. In the FFT image of Fig. 27 (b) shown in Fig. 27 (d), no clear peak corresponding to the modulation was observed, unlike the 4.2 K result shown in Fig. 27 (c). This indicates that the faint spatial modulation observed at 80 K has no coherence of the modulation along both the $a$- and $b$-axis directions. Figs. 27 (e) and (f) are inverse FFT images of the central region shown in the insets of Figs. 27 (c) and (d), respectively. The apparent lack of coherence at 80 K can be seen. In addition, the average interval of faint spatial modulation seen in the STM image at 80 K is much shorter than that at 4.2 K.
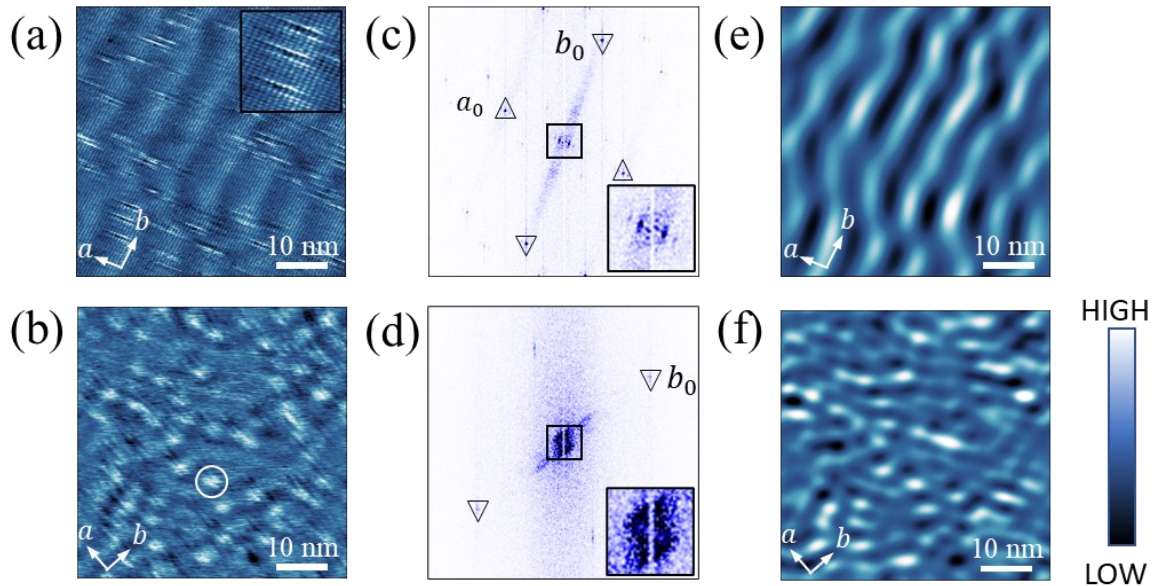


Fig. 27. (a) STM image measured at 4.2 K ($V_{\text{Bias}} = -50\,\text{mV}, I_t = 100\,\text{pA}$, 51.9×51.9 nm$^2$). Inset: The enlarged image of the area near the point defect. (b) STM image measured at 80 K ($V_{\text{Bias}} = -200\,\text{mV}$, $I_t = 100\,\text{pA}$, 51.9×51.9 nm$^2$). (c) FFT image of (a). Inset: The enlarged image of the center part. (d) FFT image of (b) Inset: The enlarged image of the center part. (e), (f) Inverse FFT images of the center part of the FFT shown in the inset of (c) and (d), respectively. © [2023] The Authors(S. Kobayashi *et al*). Originally published in JPS Conference Proceedings 38, 011053 (2023)], [Decoherence in CDW above CDW Transition Temperature in ZrTe3], [DOI: 10.7566/JPSCP.38.011053].

Furthermore, several contrast-enhanced circular regions are observed in Fig. 27 (b). One of them is marked by a white-circle. These contrast-enhanced regions appear at the locations where defects are present, and the faint spatial modulation develops from this contrast-enhanced region to connect the other contrast-enhanced regions. Appearance of such regions cannot be explained with ordinary pinning by atomic defects.

There are two possible reasons for the appearance of such contrast-enhanced regions. 1) the weak modulation is locally enhanced on the defects, or 2) the contrast of the stripe owing to the atomic defects is strengthened on the crest of the weak modulation. In any case, it is difficult to explain the observed contrast enhancement region by a simple pinning model in CDW. Previous study based on the resonant x-ray diffraction measurements have proposed that Friedel oscillation at the atomic defect grow owing to lattice soft modes near the $T_{CDW}$. Therefore, the origin of the contrast-enhanced regions observed in this study could be related to Friedel oscillation.

The disordered CDW at 80 K has already been reported by Liu *et al.*[48] However, they did not observed the contrast-enhanced region that we have observed. The possible reason of this may be the difference of the number of defects. On the surface we observed, the number of defects is higher than one of Liu *et al* reported, as seen in Figs. 27 (a) and (b). It has been reported that an increase in the amount of defects causes a decrease in $T_{CDW}$.[47] Therefore, it is possible that the surfaces on which we performed our STM measurements have locally decreased $T_{CDW}$. Consequently, the 80 K at which we performed our STM measurements may correspond to a temperature further away from the $T_{CDW}$.

The stripe structure observed near the atomic defect seems to have fine structure. The elucidation of this structure needs further investigation.

## 4.4.2 Result of Synchrotron X-ray measurement

Figure 28 (a) shows the S-XRD pattern of obtained for polycrystals at 300 K. Figure 28 (b) shows enlarged figure of Fig 28 (a). As shown in Fig 28 (b), Bragg peaks owing to $ZrTe_3$ were assigned with asterisks. Bragg peaks, which were not able to assign with asterisks, were assigned as Bragg peaks owing to $ZrTe_5$. Therefore, Rietveld analysis was performed assuming the existence of these two phases. In the analysis, we used $P2_1/m$ as the space group of $ZrTe_3$ as previously reported. The fitted profile of $ZrTe_3$ (with the $ZrTe_5$ impurity) is shown in Fig. 28. The obtained atomic positions, occupancies, and anisotropic atomic displacement parameters are summarized in Table VIII. The Rietveld analysis shows that volume fraction of $ZrTe_5$ is 35%. This yields the small confidence factors shown in the lower part of Table VII.

From this Rietveld analysis, the deficiencies of the constituent atoms are evaluated. The results are summarized in Table VIII. We found there are no defects in Zr and Te1. On the other hand, Te2 and Te3 sites show deficiencies of 4.6% and 5.8%, respectively, indicating strong site dependence. Since Te2 and Te3 are located on the cleavage planes, we can say that the defects observed in the STM are these deficiencies. Because the deficiencies of the constituent atoms are observed by the XRD measurement, we can safely conclude that the defects exist not only the cleaved

sample surface, but also in the bulk. Thus, the existence of the deficiency affects the bulk nature of $ZrTe_3$. Because Te2 and Te3 are related to the formation of the CDW, defects at these sites are strongly related to the properties of the CDW.

In addition to the existence of site selective deficiency, we found highly anisotropic atomic displacements. Figure 29 shows the anisotropic atomic displacement
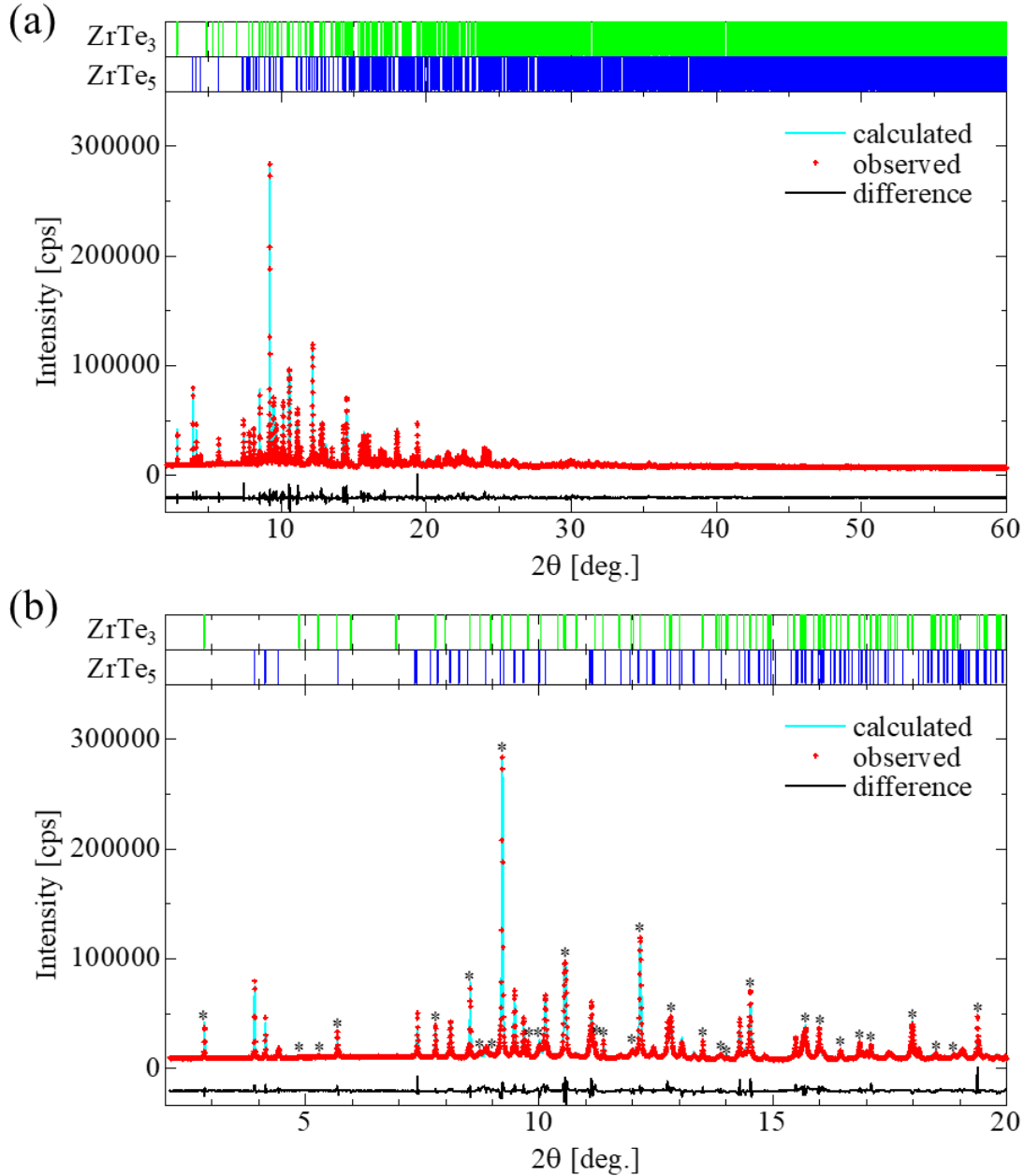


Fig. 28. XRD pattern of $ZrTe_3$ polycrystal and the results of Rietveld analysis. XRD pattern are fitted as $ZrTe_3$ and $ZrTe_5$. (a) The pattern are plotted in the range 2-60 deg. (b) The pattern are plotted in the range 2-20 deg. The asterisks are assigned $ZrTe_3$ peaks.

Table VIII. Obtained atomic coordinate (*x, y, z*), isotropic thermal paramters $B_{eq}$ and anisotropuc thermal parameters $U_{nm}$ for ZrTe$_3$ at 300 K with space group $P2_1/m$. (When calculating the change rate of $U_{31}$, the diagonal length of the parallelogram formed by the *a*-axis and *c*-axis was used as the lattice constant.)

| Atom | Site | $x$ | $y$ | $z$ | $B_{eq}$ | Occ. |
|------|------|------|------|------|------|------|
| Zr | 2e | 0.7173(11) | 1/4 | 0.3677(7) | 14.401 | 1 |
| Te1 | 2e | 0.2334(9) | 1/4 | 0.4206(5) | 10.756 | 1 |
| Te2 | 2e | 0.9095(8) | -1/4 | 0.1613(3) | 1.417 | 0.954 |
| Te3 | 2e | 0.4262(8) | -1/4 | 0.1633(3) | 1.198 | 0.942 |

| Atom | $U_{11}$ (Å$^2$) | $U_{22}$ (Å$^2$) | $U_{33}$ (Å$^2$) | $U_{31}$ (Å$^2$) |
|------|------|------|------|------|
| Zr | 0.003731 | 0.006398 | 0.538814 | 0.04462 |
| Te1 | 0.017343 | 0.007847 | 0.398662 | 0.081914 |
| Te2 | 0.015999 | 0.00144 | 0.035662 | 0.001134 |
| Te3 | 0.010462 | 0.015071 | 0.021163 | 0.006335 |

| Atom | $\sqrt{U_{11}}/a$ (%) | $\sqrt{U_{22}}/b$ (%) | $\sqrt{U_{33}}/c$ (%) | $\sqrt{U_{31}}/ac$ (%) |
|------|------|------|------|------|
| Zr | 1.03 | 2.03 | 7.26 | 1.92 |
| Te1 | 2.23 | 2.25 | 6.24 | 2.61 |
| Te2 | 2.14 | 0.96 | 1.86 | 0.30 |
| Te3 | 1.73 | 3.12 | 1.43 | 0.72 |

The temperature factor is expressed as $\exp(-2\pi^2(a^{*2}U_{11}h^2 + b^{*2}U_{22}k^2 + c^{*2}U_{33}l^2 + 2a^*b^*U_{12}hk + 2b^*c^*U_{31}hl + 2c^*a^*U_{23}lk)$. To reduce the parameters, we restricted occupancy(Zr) = occupancy(Te1) = 1. From the symmetry of space group P21/m, $U_{12}$ and $U_{23}$ are restricted as 0.
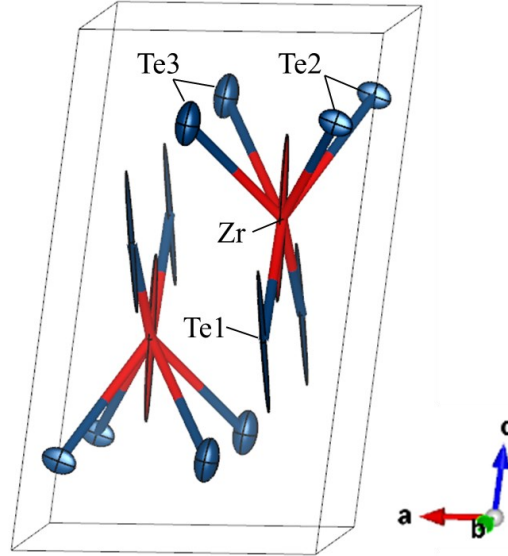


Fig. 29. Crystal structure of ZrTe$_3$ at 300 K. Each ion is shown with anisotropic ellipsoids at 300 K. The probability of anisotropic thermal ellipsoids is 99%.

parameters as ellipsoids. The atomic displacements of Te2 and Te3, which show deficiency, have rather small anisotropy. On the other hand, the atomic displacements of Zr and Te1 are highly anisotropic along the *c*-axis direction. Thus, they are shown

as needle-shape. To quantitatively evaluate the magnitude of the atomic displacements, the square root of the atomic displacement parameters divided by the lattice constant was calculated and summarized at the bottom of Table VIII. The calculated values corresponding to $U_{33}$ for Zr and Te1 are 7.26% and 6.24%, respectively. They are two times larger than those calculated for other atomic displacements.

The large atomic displacement parameter $U_{33}$ for Zr and Te1 indicates that this material is potentially unstable with the degree of freedom along the $c$-axis. It has been reported that, when this material is synthesized at high temperatures, two phases with different Zr and Te1 positions along the $c$-axis appeared.[47] This is consistent with the large atomic displacement parameter. In our Rietveld analysis, we did not obtain a small confidence factor when the existence of two phases with different Zr and Te1 positions is assumed.

## 4.5 Conclusion

STM/STS measurements were performed on a single crystal of $ZrTe_3$ at above and below $T_{CDW}$. A weak modulation was observed above $T_{CDW}$. The modulation had no phase coherence along both the CDW direction and the direction perpendicular to the CDW. Furthermore, the contrast-enhanced region was observed. The origin of this contrast-enhanced region may be related to Friedel oscillations grown near the $T_{CDW}$.

The crystal structure of $ZrTe_3$ was analyzed using S-XRD to determine the occupancy of each atomic site. About 5% of defects were found in the bulk crystal for Te2 and Te3 sites, which are located at cleavage planes observed in STM measurements, while no defects were found for Te1 and Zr.

# Chapter 5

## 5 Summary

In this paper, two objects were studied: first, crystal synthesis, characterization, and structural analysis in $LaO_{0.5}F_{0.5}BiS_2$ substituted with Sn; second, structural analysis and STM/STS measurements at 4.2 and 80 K in $ZrTe_3$.

First, it was found that substitution of Bi with Sn induces a structural phase transition from the semiconducting $P4/nmm$ phase to the metallic $P2_1/m$ phase. This is the first report of such a transition in a $BiS_2$ system under ambient pressure. Bulk SC with $T_c$ of approximately 6 K was found to occur in the vicinity of this structural phase transition. We also found a filamentary SC with $T_c$ of approximately 8 K, which is almost three times higher than that of the unsubstituted sample. This transition temperature is close to that of $LaO_{0.5}F_{0.5}BiS_2$ under high pressure, and further improvement in the transition temperature by elemental substitution is expected. However, it is still unresolved why Sn substitution causes such a structural phase transition. In addition, it was found that the composition with improved transition temperature is a mixture of $P2_1/m$ and $P4/nmm$ phases, but what is happening by the mixture is still unresolved. Future soft X-ray analyses of the domain distribution may reveal the mechanism of superconductivity in this material.

Second, real-space observations of the $ZrTe_3$ surface using STM/STS were performed above and below the $T_{CDW}$. It was found that the faint spatial modulation exists above $T_{CDW}$. This faint spatial modulation had no phase coherence in either the CDW direction or the direction perpendicular to the CDW direction. There was a contrast-enhanced region of the faint spatial modulation. The origin of this region may be related to Friedel oscillation growing near the $T_{CDW}$.

The analysis of the crystal structure of $ZrTe_3$ revealed site selective defects: only at Te2 and Te3 sites, the defects exist with approximately 5%, while the defect in Zr and Te1 sites were absent. These results provide essential information for understanding the CDW and SC in $ZrTe_3$. Going further from the discovery of selective defects, real-space observations of the $ZrTe_3$ surface using STM/STS were performed above and below the $T_{CDW}$. As a result, it was found that the faint modulation also exists above $T_{CDW}$. This faint modulation had no phase coherence in either the CDW direction or the direction perpendicular to the CDW direction. In the Te defects on the sample surface revealed by structural analysis, there was a contrast-enhanced region of the faint modulation. The origin of this region may be related to Friedel oscillation growing near the $T_{CDW}$. Because Faint spatial modulation has a size close to that of the CDW, it is likely that a defect is involved in the formation process of the CDW. In the future, similar measurements on Se-substituted $ZrTe_3$, in which the CDW has disappeared, will more certainly point out the presence of Friedel oscillations in the defects.

# Acknowledgement

I express my sincere gratitude to the numerous individuals and institutions whose invaluable support and collaboration significantly contributed to the formulation of this manuscript. Foremost, I extend my appreciation to Professor Hideaki Sakata for his mentorship in the conceptualization of experimental designs, execution of experimental procedures, data analysis, scholarly composition, and myriad other facets. His guidance, unwavering until the conclusion, is indelibly etched in my memory.

Furthermore, I extend my thanks to Assistant Professor Satoshi Demura and Assistant Professor Atsushi Nomura for their insightful contributions to the elucidation of experimental data, drawing upon their extensive knowledge and experience. They not only imparted wisdom on data interpretation but also shared their research methodologies and perspectives that will undoubtedly shape my future endeavors.

I must also acknowledge Professor Hiroshi Sawa and Mr. Takeshi Hara of Nagoya University for their counsel and experimental assistance in conducting synchrotron radiation X-ray diffraction experiments. Despite being external to our academic institution, their perspicacious insights and guidance were as profound as those of our internal peers, aiding in experiments that persisted late into the nocturnal hours. My gratitude extends to them for granting me access to the experimental apparatus at the Sawa Lab.

Appreciation is also due to my laboratory colleagues, with whom I shared substantial time, and Dr. Shun Ohta, who imparted comprehensive knowledge of experiments conducted at the Sakata Lab and facilitated extensive discussions. I extend my thanks to fellow classmates, Mr. Shohei Mori, Mr. Yuto Nakayama, Mr. Junya Tanaka, and Ms. Kanako Noguchi, with whom I collaborated. Additionally, I express gratitude to Ms. Tomoko Takeda for her unwavering support during my experimental pursuits.

I am indebted to the Tokyo University of Science for affording me the opportunity to engage with diverse individuals and undertake challenging endeavors. The institution has been instrumental in shaping my intellectual and personal growth.

# References

[1]     E. Krüger, *Constraining Forces Causing the Meissner Effect*, J. Mod. Phys. **8**, 1134 (2017).

[2]     F. London, *Superfluids, Macroscopy Theory of Supeconductivity*, Vol. I (Wiley, New York, 1950).

[3]     V. L. Ginzburg and L. D. Landau, *ON THE THEORY OF SUPERCONDUCTIVITY*, Zh. Eksp. Teor. Fiz. **20**, 1064 (1950).

[4]     J. Barden, L. Cooper, and R. Schrieffer, *Microscopic Theory of Superconductivity*, Phys. Rev. **106**, 162 (1957).

[5]     M. K. Wu, J. R. Ashburn, C. J. Torng, P. H. Hor, R. L. Meng, L. Gao, Z. J. Huang, Y. Q. Wang, and C. W. Chu, *Superconductivity at 93 K in a New Mixed-Phase Y-Ba-Cu-O Compound System at Ambient Pressure*, Phys. Rev. Lett. **58**, 908 (1987).

[6]     Z. Gao, L. Wang, Y. Qi, D. Wang, X. Zhang, Y. Ma, H. Yang, and H. Wen, *Superconducting Properties of Granular SmFeAsO1−xFx Wires with Tc = 52 K Prepared by the Powder-in-Tube Method*, Supercond. Sci. Technol. **21**, 112001 (2008).

[7]     R. Peierls, *The Size of a Dislocation*, Proc. Phys. Soc. **52**, 34 (1940).

[8]     G. Grüner, *The Dynamics of Charge-Density Waves*, Rev. Mod. Phys. **60**, 1129 (1988).

[9]     G. Binnig and H. Rohrer, *Scanning Tunneling Microscopy*, Surf. Sci. **152–153**, 17 (1985).

[10]    S. H. Pan, E. W. Hudson, and J. C. Davis, *3He Refrigerator Based Very Low Temperature Scanning Tunneling Microscope*, Rev. Sci. Instrum. **70**, 1459 (1999).

[11]    Y. Mizuguchi, S. Demura, K. Deguchi, Y. Takano, H. Fujihisa, Y. Gotoh, H. Izawa, and O. Miura, *Superconductivity in Novel BiS2-Based Layered Superconductor LaO1-XFxBiS2*, J. Phys. Soc. Jpn. **81**, 114725 (2012).

[12]    Y. Mizuguchi, *Review of Superconductivity in BiS2-Based Layered Materials*, J. Phys. Chem. Solids **84**, 34 (2015).

[13]    Y. Mizuguchi, *Material Development and Physical Properties of BiS2-Based Layered Compounds*, J. Phys. Soc. Jpn. **88**, 041001 (2019).

[14]    J. Xing, S. Li, X. Ding, H. Yang, and H.-H. Wen, *Superconductivity Appears in the Vicinity of Semiconducting-like Behavior in CeO₋XF$_x$BiS$_2$*, Phys. Rev. B **86**, 214518 (2012).

[15]    R. Jha, A. Kumar, S. Kumar Singh, and V. P. S. Awana, *Synthesis and Superconductivity of New BiS2 Based Superconductor PrO0.5F0.5BiS2*, J. Supercond. Novel Magn. **26**, 499 (2013).

[16]    M. Nagao, S. Demura, K. Deguchi, A. Miura, S. Watauchi, T. Takei, Y. Takano, N. Kumada, and I. Tanaka, *Structural Analysis and Superconducting Properties of F-Substituted NdOBiS2 Single Crystals*, J. Phys. Soc. Jpn. **82**, 113701 (2013).

[17]    D. Yazici, K. Huang, B. D. White, A. H. Chang, A. J. Friedman, and M. B. Maple, *Superconductivity of F-Substituted LnOBiS2 (Ln=La, Ce, Pr, Nd, Yb) Compounds*, Philos. Mag. **93**, 673 (2013).

[18]    S. Demura et al., *Coexistence of Bulk Superconductivity and Magnetism in CeO1−xFxBiS2*, J. Phys. Soc. Jpn. **84**, 024709 (2015).

[19]     G. S. Thakur, G. K. Selvan, Z. Haque, L. C. Gupta, S. L. Samal, S. Arumugam, and A. K. Ganguli, *Synthesis and Properties of SmO0.5F0.5BiS2 and Enhancement in Tc in La1−YSmyO0.5F0.5BiS2*, Inorg. Chem. **54**, 1076 (2015).

[20]     B. Li, Z. W. Xing, and G. Q. Huang, *Phonon Spectra and Superconductivity of the BiS2-Based Compounds LaO1−xFxBiS2*, EPL **101**, 47002 (2013).

[21]     T. Tomita et al., *Pressure-Induced Enhancement of Superconductivity and Structural Transition in BiS2-Layered LaO1−xFxBiS2*, J. Phys. Soc. Jpn. **83**, 063704 (2014).

[22]     S. Demura, Y. Fujisawa, S. Otsuki, R. Ishio, Y. Takano, and H. Sakata, *Enhancement of Tc in BiS2-Based Superconductors NdO0.7F0.3BiS2 by Substitution of Pb for Bi*, Solid State Commun. **223**, 40 (2015).

[23]     T. Hiroi, J. Kajitani, A. Omachi, O. Miura, and Y. Mizuguchi, *Evolution of Superconductivity in BiS2-Based Superconductor LaO0.5F0.5Bi(S1−xSex)2*, J. Phys. Soc. Jpn. **84**, 024723 (2015).

[24]     Y. Mizuguchi, A. Miura, J. Kajitani, T. Hiroi, O. Miura, K. Tadanaga, N. Kumada, E. Magome, C. Moriyoshi, and Y. Kuroiwa, *In-Plane Chemical Pressure Essential for Superconductivity in BiCh2-Based (Ch: S, Se) Layered Structure*, Sci. Rep. **5**, 14968 (2015).

[25]     S. Otsuki, S. Demura, Y. Sakai, Y. Fujisawa, and H. Sakata, *Effect of Lead Substitution on LaO0.5F0.5BiS2*, Solid State Commun. **270**, 17 (2018).

[26]     K. Sugimoto et al., *Extremely High Resolution Single Crystal Diffractometory for Orbital Resolution Using High Energy Synchrotron Radiation at SPring-8*, **1234**, 887 (2010).

[27]     G. M. Sheldrick, *Crystal Structure Refinement with SHELXL*, Acta Cryst. Section C **71**, 3 (2015).

[28]     K. Momma and F. Izumi, *VESTA 3 for Three-Dimensional Visualization of Crystal, Volumetric and Morphology Data*, J. Appl. Cryst. **44**, 1272 (2011).

[29]     E. Nishibori, M. Takata, K. Kato, M. Sakata, Y. Kubota, S. Aoyagi, Y. Kuroiwa, M. Yamakata, and N. Ikeda, *The Large Debye−Scherrer Camera Installed at SPring-8 BL02B2 for Charge Density Studies*, J. Phys. Chem. Solids **62**, 2095 (2001).

[30]     S. Kawaguchi, M. Takemoto, K. Osaka, E. Nishibori, C. Moriyoshi, Y. Kubota, Y. Kuroiwa, and K. Sugimoto, *High-Throughput Powder Diffraction Measurement System Consisting of Multiple MYTHEN Detectors at Beamline BL02B2 of SPring-8*, Rev. Sci. Instrum. **88**, 085111 (2017).

[31]     S. Kawaguchi, M. Takemoto, H. Tanaka, S. Hiraide, K. Sugimoto, and Y. Kubota, *Fast Continuous Measurement of Synchrotron Powder Diffraction Synchronized with Controlling Gas and Vapour Pressures at Beamline BL02B2 of SPring-8*, J. Synchrotron Radiat. **27**, 616 (2020).

[32]     A. Altomare, C. Cuocci, C. Giacovazzo, A. Moliterni, R. Rizzi, N. Corriero, and A. Falcicchio, *EXPO2013: A Kit of Tools for Phasing Crystal Structures from Powder Data*, J. Appl. Crystallogr. **46**, 1231 (2013).

[33]     A. Miura, M. Nagao, T. Takei, S. Watauchi, I. Tanaka, and N. Kumada, *Crystal Structures of LaO1−xFxBiS2 (X~0.23, 0.46): Effect of F Doping on Distortion of Bi−S Plane*, J. Solid State Chem. **212**, 213 (2014).

[34]     S. Demura, N. Ishida, Y. Fujisawa, and H. Sakata, *Evaluation of Bi Defect Concentration in LnO1-XFxBiCh2 by Scanning Tunneling Microscopy*, J. Phys.: Conf. Ser. **871**, 012006 (2017).

[35]     R. Sagayama, H. Sagayama, R. Kumai, Y. Murakami, T. Asano, J. Kajitani, R. Higashinaka, T. D. Matsuda, and Y. Aoki, *Symmetry Lowering in*

*LaOBiS2: A Mother Material for BiS2-Based Layered Superconductors*, J. Phys. Soc. Jpn. **84**, 123703 (2015).

[36]    S. Iwasaki et al., *Anomalous Transport Properties in BiS2-Based Superconductors LnO1−xFxBiS2 (Ln = Nd, La-Sm)*, J. Phys. Soc. Jpn. **88**, 041005 (2019).

[37]    H. Usui, K. Suzuki, and K. Kuroki, *Minimal Electronic Models for Superconducting BiS$_2$ Layers*, Phys. Rev. B **86**, 220501(R) (2012).

[38]    K. Suzuki, H. Usui, K. Kuroki, and H. Ikeda, *Charge and Quadrupole Fluctuations and Gap Anisotropy in BiS$_2$-Based Superconductors*, Phys. Rev. B **96**, 024513 (2017).

[39]    Y. Li et al., *Incorporation Site and Valence State of Sn Atoms in Sn-Substituted La(O,F)BiS2 Superconductor*, J. Phys. Soc. Jpn. **91**, 054602 (2022).

[40]    S. Furuseth and H. Fjellvåg, *Re-Examination of the Crystal Structure of ZrTe3*, Acta Chem. Scand. **45**, 694 (1991).

[41]    H. Nakajima, K. Nomura, and T. Sambongi, *ANISOTROPIC SUPERCONDUCTING TRANSITION IN ZrTe3*, Proceedings of the Yamada Conference XV on Physics and Chemistry of Quasi One-Dimensional Conductors 240 (1986).

[42]    D. J. Eaglesham, J. W. Steeds, and J. A. Wilson, *Electron Microscope Study of Superlattices in ZrTe3*, J. Phys. C: Solid State Phys. **17**, L697 (1984).

[43]    M. D. Randle, A. Lipatov, I. Mansaray, J. E. Han, A. Sinitskii, and J. P. Bird, *Collective States and Charge Density Waves in the Group IV Transition Metal Trichalcogenides*, Appl. Phys. Lett. **118**, 210502 (2021).

[44]    K. Yamaya, S. Takayanagi, and S. Tanda, *Mixed Bulk-Filament Nature in Superconductivity of the Charge-Density-Wave Conductor ZrTe3*, Phys. Rev. B **85**, 184513 (2012).

[45]    S. Tsuchiya, K. Matsubayashi, K. Yamaya, S. Takayanagi, S. Tanda, and Y. Uwatoko, *Effects of Pressure and Magnetic Field on Superconductivity in ZrTe3: Local Pair-Induced Superconductivity*, New J. Phys. **19**, 063004 (2017).

[46]    X. Zhu et al., *Superconductivity and Charge Density Wave in ZrTe3-XSex*, Sci. Rep. **6**, 26974 (2016).

[47]    X. Zhu, B. Lv, F. Wei, Y. Xue, B. Lorenz, L. Deng, Y. Sun, and C.-W. Chu, *Disorder-Induced Bulk Superconductivity in ZrTe$_3$ Single Crystals via Growth Control*, Phys. Rev. B **87**, 024508 (2013).

[48]    L. Liu et al., *Thermal Dynamics of Charge Density Wave Pinning in ZrTe3*, Phys. Rev. Lett. **126**, 256401 (2021).

[49]    L. Yue et al., *Distinction between Pristine and Disorder-Perturbed Charge Density Waves in ZrTe3*, Nat. Commun. **11**, 98 (2020).

[50]    A. Nomura, S. Kobayashi, S. Ohta, and H. Sakata, *Relationship between Charge Density Wave, Filamentary Superconductivity and Bulk Superconductivity in ZrTe3*, EPL **133**, 37003 (2021).

[51]    F. Izumi and K. Momma, *Three-Dimensional Visualization in Powder Diffraction*, Solid State Phenom. **130**, 15 (2007).

[52]    T. Yokoya, T. Kiss, A. Chainani, S. Shin, and K. Yamaya, *Role of Charge-Density-Wave Fluctuations on the Spectral Function in a Metallic Charge-Density-Wave System*, Phys. Rev. B **71**, 140504 (2005).